2010

Issures in Discontinuous High-Order Methods: Broadband Wave Computation and Viscous Boundary Layer Resolution

Yi Li
Iowa State University

Issues in discontinuous high-order methods: Broadband wave computation and viscous boundary layer resolution

by

Yi Li

A dissertation submitted to the graduate faculty

in partial fulfillment of the requirements for the degree of

DOCTOR OF PHILOSOPHY

Major: Aerospace Engineering

Program of Study Committee:
Z.J. Wang, Major Professor
Thomas J Rudolphi
Alric R Rothmayer
Ambar K Mitra
Hailiang Liu

Iowa State University

Ames, Iowa

2010

DEDICATION

To My Parents

TABLE OF CONTENTS

LIST OF FIGURES

LIST OF TABLES

ACKNOWLEDGEMENTS

I would like to take this opportunity to express my thanks to those who helped me with various aspects of conducting research and the writing of this thesis.

First and foremost, I would like to thank Dr. Z.J. Wang for his guidance, patience and support throughout this research and the writing of this thesis. His insights and knowledge have often inspired me and renewed my hopes for completing my graduate education. I feel grateful to have this chance to work on this thesis under his supervision.

I would also like to thank my committee members for their efforts and contributions to this work: Dr. Rudolphi, Thomas J, Dr. Rothmayer, Alric P, Dr. Mitra, Ambar K and Dr. Liu hailiang. I would additionally like to thank Dr. Tom Shih from Purdue University for his advice and kind help.

My sincere thanks extend to Haiyang Gao, Takanori Haga, Ying Zhou, Varun Vikas, Meilin Yu and other co-workers and friends, for their time and advice in this thesis preparation. My special thanks are to Kris Van Den Abeele from Vrije Universiteit Brussel for knowledgeable help and his time.

Finally I would like to express my deepest love and thanks to my family for their love and continuous support.

ABSTRACT

A new discontinuous formulation named Correction Procedure via Reconstruction (CPR) was developed by Huynh [49] in 1D, and extended to simplex and hybrid meshes by Wang & Gao [107] for conservation laws. As with all discontinuous methods such as the discontinuous Galerkin (DG), spectral volume (SV) and spectral difference (SD) methods, CPR method employs a piecewise discontinuous space. All of them can be unified under the CPR framework, which is relatively simple to implement especially for high-order elements. In this thesis, we deal with two issues: the efficient computation of broadband waves, and the proper resolution of a viscous boundary layer with the high-order CPR method.

A hybrid discontinuous space including polynomial and Fourier bases is employed in the CPR formulation in order to compute broad-band waves. The polynomial bases are used to achieve a certain order of accuracy, while the Fourier bases are able to exactly resolve waves at a certain frequency. Free-parameters introduced in the Fourier bases are optimized in order to minimize both dispersion and dissipation errors by mimicking the dispersion-relation-preserving (DRP) method for a one-dimensional wave problem.

For the one-dimensional wave problem, the dispersion and dissipation properties and the optimization procedure are investigated through a wave propagation analysis. The optimization procedure is verified with a wave propagation analysis. This optimization procedure is verified through a mesh resolution analysis, which gives the relation between the grid points-per-wavelength (PPW) and the wave propagation distance. Numerical tests have been performed to verify the wave propagation properties for the scalar advection equation. The two-dimensional wave behavior is investigated through a wave propagation

analysis too. The wave propagation properties are verified with a numerical test of the two-dimensional acoustic wave equation.

In order to understand the mesh size requirement to resolve a viscous boundary layer using high-order methods, extensive grid resolution studies are performed for both 1D and 2D viscous burger's equations with exact solutions. The skin friction is used as an indicator of accuracy for the resolution of a boundary layer. For the diffusion terms, the local discontinuous Galerkin (LDG) method is employed to achieve the $(k+1)th$ order of accuracy with a degree k polynomial reconstruction.

For the 1D viscous burger's equation, different grid sizes are determined for various order CPR formulations given a certain error in the skin friction. And different skin frictions are obtained for a certain grid size. In addition, accuracy and convergence properties are studied for different distribution of solution points.

A 2D viscous burger's equation with an exact solution is designed to test the resolution for various orders of CPR formulations. The method of manufactured solution (MMS) is employed to provide an exact solution for code accuracy verification. In MMS, instead of solving the original equation directly, the equation with an analytical source term is solved. Accuracy studies are also carried out.

Keywords: (Correction Procedure via Reconstruction), A Hybrid Discontinuous Space, Wave Propagation Analysis, Grid Resolution Study, Method of Manufactured Solution.

CHAPTER 1. INTRODUCTION

1.1 Overview of High-Order Methods

Computational fluid dynamics (CFD) has been made impressive progress over the past decades, due to advances in many fields including numerical solution techniques and computer science and engineering. CFD tools are becoming more and more useful as current computer hardware makes the simulation of complex fluid flow not only feasible, but also economical. Nowadays, nearly all commercial CFD solvers are based on second-order accurate numerical methods, either finite volume (FV) [1, 2, 7], finite difference (FD) [17, 37, 77] or finite element [16, 40, 45-47, 66]. The Reynolds averaged Navier-Stokes (RANs) equations can be solved for "real world" configurations within a few hours on parallel computing system.

Although these second-order solvers have proven very useful, they are insufficient to accurately predict many flow problems such as wave propagation problems, vortex-dominated flows, as well as large eddy simulation and direction numerical simulation (DNS) of turbulence. Second-order algorithms are mostly too dissipative to resolve these problems accurately. High-order methods are more suited for such applications, since they have much better wave propagation properties.

High-order accuracy can be achieved with FV method on structured grids, by extending the stencil that is used for the reconstruction of the solution variables at the cell faces. However, the generation of structured grids is difficult for complicated geometries. On the other hand, the generation of unstructured grids is much easier and can be automated. High-order methods suited for unstructured grids are required. Such methods approximate the

solution by constructing a high-order polynomial of a certain degree on each cell. They are compact methods because only local data on each cell and data of its immediate neighbors is required for the evaluation of the fluxes, which makes such methods easily parallelizable. The discontinuous Galerkin (DG), spectral volume (SV) and spectral difference (SD) methods belong to the class of methods. An overview of DG, SV and SD methods is presented here. A new discontinuous formulation named the Correction Procedure via Reconstruction (CPR) was developed on hybrid meshes, which shows more efficient implementation especially for high-order elements.

1.1.1 Discontinuous Galerkin (DG) Method

The DG method as the most popular high-order method for unstructured girds is locally conservative, high-order accurate and can easily handle irregular meshes for complex geometries. It was introduced by Reed and Hill [74] in 1973 for solving a steady conservation law, namely the neutron transport equation. It was first used for unsteady advection laws by Van Leer [94] in 1978. Important contributions to the development of the DG method for hyperbolic conservation laws were made by Cockburn, Shu et al. [24-27], with the development of the Runge-Kutta DG (RKDG) methods. A comprehensive overview of these RKDG methods can be found in a review article by Cockburn and Shu [29]. Bassi and Rebay demonstrated the DG method for the compressible Euler and N-S equations in obtaining high-order accuracy [9, 10, 13].

The DG method has been extended to solve the diffusion equation and the diffusive terms of the N-S equations. These approaches include interior penalty (IP) approaches, see e.g. Douglas and Dupont [33], the approach by Baumann and Oden [14-15] and the local DG

approach by Cockburn and Shu [28], different approaches by Bassi et al. [11, 8] and the recovery methods by Van Leer et al. [95-97]. Readers who are interested in these approaches can refer to an overview by Arnold et al. [3], where their consistency, stability and order of accuracy are discussed. The order of accuracy of all these approaches for the diffusion equation is limited to $k+1$, with the degree k polynomial. Van Leer et al. developed the recovery methods and the suboptimal based on a better understanding of the physical nature of the diffusion equation, which are capable of achieving higher orders of accuracy up to $2k+2$. There recovery methods do not fit inside the unifying framework proposed by Arnold et al. [3].

Many other researchers made significant contributions to the DG method. A quadrature-free DG formulation was developed by Atkins and Shu [5]. Hu et al. [43] performed an analysis of the wave propagation properties of the DG method. A simplified treatment of curved wall boundaries for the Euler equations with the DG method was proposed by Krivodonova and Berger [59]. Space-time implicit DG methods for hyperbolic conservation laws were presented by Lowrie et al. [68], Van der Vegt and Van der Ven [93], and Klaij et al. [55]. General overviews of the DG method can be found in lecture notes by Cockburn et al. [21] and by Hartmann [39].

1.1.2 Spectral Volume (SV) and Spectral Difference (SD) Method

The basic methodology of the SV method was first presented by Wang [100], along with its application to one-dimensional scalar hyperbolic conservation laws in 2002. The SV method was extended to two-dimensional scalar equations and different limiting strategies were studied to capture discontinuous solutions by Wang and Liu [101]. The SV method was

extended to one-dimensional systems of conservation laws, along with an optimization study of the SV partitions in [102]. The SV was applied to solve two-dimensional inviscid flow problems, governed by the 2D Euler equations, by Wang et al. [103]. The appropriate treatment of curved wall boundaries was addressed for 2D SV method by Wang and Liu [105], by using a high-order geometric mapping of the SV cells near wall boundaries. The extension to three-dimensional systems of conservation laws was then carried out by Liu et al. [64], who applied the SV method to 3D computational electromagnetics (CEM) problems. Sun et al. [80] developed and presented a formulation of the SV method for the N-S equations. Haga et al. solved 3D Euler and N-S equations with the SV method on Japan‘s Earth Simulator Computer. Kannan et al [53] investigated different formulations for the discretization of diffusive terms with the SV method. Comparison of the SV method with the DG method were made by Sun and Wang [82] and Zhang and Shu [114]. A quadrature-free formulation of the SV method in analogy with the quadrature-free formulation of the DG method was developed by Harris et al. [36], is more efficient than the standard formulation in terms of computational time.

Chen [18-19] made a contribution towards the appropriate definition of high-order accurate SV partitions of simplex cells based on the Lebesgue constant criterion formulated by Wang and Liu [101]. Van Den Abeele et al. [86-88, 90, 92] performed Fourier analysis for 1D, 2D and 3D SV partitions of the simplex cells to assess the accuracy and stability properties of the SV schemes. Harris and Wang [36] coupled this analysis to an optimization algorithm to identify optimal SV partitions.

The first work on the method which is known as the SD method dates on 1996 and is due to Kopriva and Kolias [58] and Kopriva [57], who called the method ‘conservative

staggered-grid Chebyshev multidomain method'. Their formulation was for quadrilateral cells and they solved two-dimensional compressible flow problems based on the Euler equations. A general formulation of the method, including simplex cells, was given in 2006 by Liu et al. [65], who first called it SD method, and applied it to two-dimensional scalar conservation laws and CEM problems. The SD method for simplex cells was then successfully extended to the 2D Euler equations by Wang et al. [104] and to the 2D N-S equations by May and Jameson [70] and Wang et al. [108]. An implementation of the SD method on hexahedral cells for the 3D N-S equations was reported by Sun et al. [83]. Different approaches for the discretization of the diffusive terms in the N-S equations with the SD method, were investigated by Van den Abeele et al. [91]. Huang et al. [44] reported an implicit space-time implementation of the SD method. Van den Abeele et al. proved that the SD method is independent of the positions of its solution points and found that 1D SV and SD methods are equivalent. Huynh [49] proposed a set of 1D SV and SD schemes based on Legendre-Gauss quadrature points and Jameson proved that these are stable for arbitrary orders of accuracy [70].

1.1.3 Correction Procedure via Reconstruction (CPR) Method

Recently, a new differential discontinuous formulation for conservation laws named the Correction Procedure via Reconstruction (CPR) is developed on hybrid meshes [107], which is inspired by several other discontinuous methods such as the DG, SG (staggered grid multi-domain), SV and SD methods. All of them can be unified under the CPR framework, which was relatively simple to implement especially for high-order elements.

The CPR formulation was developed in [107] under the name of flux reconstruction (FR) [49] and under the name of lifting collocation penalty (LCP). The LCP formulation is directly inspired by the FR method and can be viewed as an extension of the original FR method to simplex elements. Instead of directly reconstructing the flux function, a "correction field" due to interface flux jumps is computed in LCP. These two formulations have been renamed CPR, which is referred to FR and LCP.

The degrees-of-freedom (DOFs) are the state variables named solution points (SPs) in the CPR formulation, where the differential form of the governing equation is solved. As a result, explicit surface and volume integrals are avoided. The CPR formulation is among the most efficient discontinuous methods in terms of the number of operations. The CPR framework is given in the next chapter.

1.2 Objectives of the Present Work

In this thesis, two issues are addressed for the CPR method. One is the efficient computation of broadband waves, another is the proper resolution of a viscous boundary layer with the high-order CPR method.

1.2.1 Computation of Broad-band Wave

The stability and accuracy of the CPR method depend on the choice of the solution approximation space and weighting functions. The basis function should be specified to define a CPR scheme. Mostly, the space of polynomial with degree k or less is chosen, which leads to a $(k+1)th$ order accuracy scheme for convection equations. In the present study, hybrid bases including polynomial and Fourier bases are introduced as the local

approximation space in order to better resolve broadband wave propagation problems. Fourier bases are used such that the CPR scheme can exactly simulate a wave equation for certain wave numbers and resolve broadband wave numbers, and polynomial bases are kept with the objective of achieving a given order of accuracy.

We borrow the ideas from the central and upwind dispersion-Relation-Preserving (DRP) schemes in determining the parameters of the Fourier bases to maximize the resolvable wave numbers given a certain error threshold [84, 85]. The basic idea of DRP scheme is to optimize the scheme coefficients for the high resolution of short waves with respect to the computational grid instead of the truncation errors. The optimization process has to allow the normalized L_2 norm of both dispersion and dissipation errors to be as close to zero as possible for a certain integration number range. This method is named a frequency optimized CPR formulation (FOCPR).

The Fourier analysis is performed to assess the accuracy and stability properties of the CPR schemes with hybrid bases, by following the methods by Hu [43] and Van den Abeele [86]. Mesh resolution analysis is presented to study the dependence of points-per-wavelength (PPW) requirement on the number of wavelengths, by mimicking the procedures in [110]. Numerical tests are performed which show that the CPR schemes with optimized Fourier bases can resolve waves more accurately than the classic polynomial bases.

1.2.2 Resolution of Viscous Boundary Layer

The resolution of viscous boundary layers is studied in 1D and 2D for the high-order CPR method. The space of polynomial with degree k is applied as the weighting function, which should be $(k+1)th$ order accuracy scheme for convection equations.

The different formulations play an important role for the diffusion equation simulation [79, 113]. Most of them are derived from similar approaches developed for the DG method, which can be found in Arnold et al. [3]. The most popular three approaches are applied in high-order CPR method, which are based on the Local DG (LDG) approach proposed by Cockburn and Shu [28],the first and second approaches of Bassi and Rebay (BR1 [9]) proposed by Bassi and Rebay. The order of accuracy study is performed for the different diffusion approaches to investigate their properties.

For both 1D and 2D viscous burger's equation, the skin frictions are studied as the resolution criteria. Numerical skin frictions are compared with the exact skin frictions for various orders of CPR schemes.

For 2D viscous burger's equation, the method of manufactured solution (MMS) provides a general exact solution for accuracy verification. In MMS, instead of solving the original equation directly, the equation with an analytical source term is solved. In the present study, only tensor products of one-dimensional polynomial are applied on rectangular meshes.

1.3 Outline of the Thesis

The outline of the remainder of this thesis is as follows. In chapter 2, the framework of the CPR method is given. In chapter 3, free-parameters introduced by Fourier bases are optimized by mimicking the procedure of DRP to minimize both dispersion and dissipation errors for the CPR schemes. An extensive study of the stability and accuracy properties of the CPR schemes with hybrid bases is presented. A mesh resolution analysis is performed to verify the optimization procedure. Several numerical testes are performed to verify the Fourier analysis. In chapter 4, the two-dimensional wave propagation analysis is studied

based on structured quadrilateral grids with tensor product bases. A two-dimensional acoustic wave is used to test the two-dimensional wave propagation analysis. In chapter 5, the resolution of viscous boundary layers is studied in 1D and 2D for the high-order CPR method. The skin frictions are studied as the resolution criteria for both 1D and 2D viscous burger's equation. Conclusion remarks are given and future works are presented in chapter 6.

CHAPTER 2. CORRECTION PROCEDURE VIA RECONSTRUCTION

The differential discontinuous formulation for conservation laws named the Correction Procedure via Reconstruction (CPR) was developed to improve the efficiency or stability of several well-known high-order methods, including the DG method, staggered grid multi-domain (SG), SV and SD methods. It unified all these methods into a simple nodal or collocation-type differential formulation. There is a one to one connection between different formulation and special polynomials in 1D or multiple dimensions with a tensor-product basis.

2.1 Framework of CPR formulation

The CPR formulation can be derived from a weighted residual method by transforming the integral formulation into a differential one. The hyperbolic conservation law can be written as

$$\frac{\partial Q}{\partial t} + \nabla \cdot \vec{F}(Q) = 0 \tag{2.1}$$

with proper initial and boundary conditions, where Q is the state vector, and $\vec{F}$ is the flux vector. The computation domain Ω is discretized into N non-overlapping triangular elements $\{V_i\}_{i=1}^{N}$. Let W be an arbitrary weighting function or test function. Multiplying Eq. (2.1) with an arbitrary weighting function W and integrating over an element V_i, we obtain

$$\int_{V_i} \left(\frac{\partial Q}{\partial t} + \nabla \cdot \vec{F}(Q) \right) W dV = \int_{V_i} \frac{\partial Q}{\partial t} W dV + \int_{\partial V_i} W \vec{F}(Q) \cdot \vec{n} ds - \int_{V_i} \nabla W \cdot \vec{F}(Q) dV = 0 \tag{2.2}$$

Let Q_i be an approximate solution to the analytical solution Q on element V_i. On each element, we assume that the solution belongs to the space of polynomials of degree k or less, i.e., $Q_i \in P^k(V_i)$, (or P^k if there is no confusion) with no continuity requirement across elements interfaces. Let the dimension of P^k be $K = (k+1)(k+2)/2$. In addition, the numerical solution Q_i is required to satisfy Eq. (2.2)

$$\int_{V_i} \frac{\partial Q_i}{\partial t} W dV + \int_{\partial V_i} W \vec{F}(Q_i) \cdot \vec{n} dS - \int_{V_i} \nabla W \cdot \vec{F}(Q_i) dV = 0 \tag{2.3}$$

The surface integral is not properly defined because the numerical solution is discontinuous across element interfaces. Following the idea used in the Godunov method, the normal flux term in Eq. (2.3) is replaced with a common Riemann flux, e.g.,

$$F^n(Q_i) \equiv \vec{F}(Q_i) \cdot \vec{n} \approx F^n_{com}(Q_i, Q_{i+}, \vec{n}) \tag{2.4}$$

where Q_{i+} denotes the solution outside the current element V_i. Instead of Eq. (2.3), the approximate solution is required to satisfy

$$\int_{V_i} \frac{\partial Q_i}{\partial t} W dV + \int_{\partial V_i} W F^n_{com}(Q_i, Q_{i+}, \vec{n}) dS - \int_{V_i} \nabla W \cdot \vec{F}(Q_i) dV = 0 \tag{2.5}$$

Applying integration by parts again to the last term of the above LHS, we obtain

$$\int_{V_i} \frac{\partial Q_i}{\partial t} W dV + \int_{V_i} W \nabla \cdot \vec{F}(Q_i) dV + \int_{\partial V_i} W \left[F^n_{com}(Q_i, Q_{i+}, \vec{n}) - F^n(Q_i)\right] dS = 0 \tag{2.6}$$

Here, the test space has the same dimension as the solution space, and is chosen in a manner to guarantee the existence and uniqueness of the numerical solution.

Note that the quantity $\nabla \cdot \vec{F}(Q_i)$ involves no influence from the data in the neighboring cells. The influence of these data is represented by the above boundary integral, which is also called a "penalty term", penalizing the normal flux differences.

The next step is critical in the elimination of the test function. The boundary integral above is cast as a volume integral via the introduction of a "correction field" on V_i, $\delta_i \in P^k(V_i)$,

$$\int_{V_i} W\delta_i dV = \int_{\partial V_i} W[F^n]ds \tag{2.7}$$

where $[F^n] = F^n_{com}(Q_i\ , Q_{i+}, \vec{n}) - F^n(Q_i\ )$ is the normal flux difference. The above equation is sometimes referred to as the "lifting operator", which has the normal flux differences on the boundary as input and a member of $P^k(V_i)$ as output. Substituting Eq. (2.7) into Eq. (2.6), we obtain

$$\int_{V_i} \left[\frac{\partial Q_i}{\partial t} + \nabla\cdot\vec{F}(Q_i\ ) + \delta_i\ \right] W dV = 0 \tag{2.8}$$

If the flux vector is a linear function of the state variable, then $\nabla\cdot\vec{F}(Q_i\ ) \in P^k$. In this case, the terms inside the square bracket are all elements of P^k. Because the test space is selected to ensure a unique solution, Eq. (2.8) is equivalent to

$$\frac{\partial Q_i}{\partial t} + \nabla\cdot\vec{F}(Q_i\ ) + \delta_i\ = 0 \tag{2.9}$$

For nonlinear conservation laws, $\nabla\cdot\vec{F}(Q_i\ )$ is usually not an element of P^k. As a result, Eq. (2.8) cannot be reduced to Eq. (2.9). In this case, the most obviously choice is to project $\nabla\cdot\vec{F}(Q_i\ )$ into P^k. Denote $\Pi\left(\nabla\cdot\vec{F}(Q_i\ )\right)$ a projection of $\nabla\cdot\vec{F}(Q_i\ )$ to P^k. Once choice is

$$\int_{V_i} \Pi\left(\nabla\cdot\vec{F}(Q_i\ )\right) W dV = \int_{V_i} \nabla\cdot\vec{F}(Q_i\ ) W dV \tag{2.10}$$

Then Eq. (8) reduces to

$$\frac{\partial Q_i}{\partial t} + \Pi\left(\nabla \cdot \vec{F}\left(Q_i\right)\right) + \delta_i = 0 \tag{2.11}$$

with the introduction of the correction field δ_i, and a projection of $\Pi\left(\nabla \cdot \vec{F}\left(Q_i\right)\right)$ for nonlinear conservation laws, we have reduced the weighted residual formulation to a different formulation, which involves no integrals. Note that for δ_i defined by Eq. (2.7), if $W \in P^k$, Eq. (2.11) is equivalent to the DG formulation, at least for linear conservation laws; if W belongs to another space, the resulting δ_i is different. We obtain a formulation corresponding to a different method such as the SV method.

Next, let the DOFs be the solutions at a set of solution points (SPs) $\{\vec{r}_{ij}\}$ (j varies from 1 to K), as shown in Fig 2.1. Then Eq. (2.11) holds true at the SPs, i.e.,

$$\frac{\partial Q_{i,j}}{\partial t} + \Pi_j\left(\nabla \cdot \vec{F}\left(Q_i\right)\right) + \delta_{i,j} = 0 \tag{2.12}$$

where $\Pi_j\left(\nabla \cdot \vec{F}\left(Q_i\right)\right)$ denotes the values of $\Pi\left(\nabla \cdot \vec{F}\left(Q_i\right)\right)$ at SP j. The efficiency of the CPR approach hinges on how the correction field δ_i and the projection $\Pi\left(\nabla \cdot \vec{F}\left(Q_i\right)\right)$ are computed. To compute δ_i, we define $k+1$ points named flux points (FPs) along each interface, where the normal flux differences $[F^n]$ are computed, as shown in Fig 2.1. We approximate (for nonlinear conservation laws) the normal flux difference $[F^n]$ with a degree k interpolation polynomial along each interface,

$$[F^n]_f \approx \boldsymbol{I}_k[F^n]_f \equiv \sum_l [F^n]_{f,l} L_l^{FP} \tag{2.13}$$

where f is an face (or edge in 2D) index, and l is the FP index, and L_l^{FP} is the Lagrange interpolation polynomial based on the FPs in a local interface coordinate. For linear triangles

with straight edges, once the solutions points and flux points are chosen, the correction at the SPs can be written as

$$\delta_{i,j} = \frac{1}{|V_i|} \sum_{f \in \partial V_i} \sum_{l} \alpha_{j,f,l} [F^n]_{f,l} S_f \tag{2.14}$$

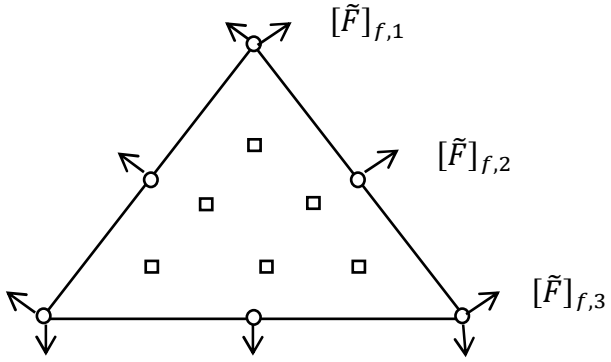

Figure 2.1. Solution points (squares) and flux points (circles) for a triangular element of

$$k = 2$$

where $\alpha_{j,f,l}$ are lifting constants independent of the solution, S_f is the face area, $|V_i|$ is the volume of V_i. Note that the correction for each solution point, namely $\delta_{i,j}$, is a linear combination of all the normal flux differences on all the faces of the cell. Conversely, a normal flux difference at a flux point on a face, say (f, l) results in a correction at a solution pint j of an amount $\alpha_{j,f,l}[F^n]_{f,l} S_f / |V_i|$.

Next, we focus on how to compute $\Pi_j \left(\nabla \cdot \vec{F}(Q_i) \right)$ efficiently. A brute-force implementation based on Eq. (2.10) requires high-order integral quadratures, and is expensive. Two more efficient approaches are developed in Ref. 42, and reviewed here for the sake of completeness.

Based on the solution at a SP, the flux vector at each SP can be computed. Then a degree k Lagrange interpolation polynomial for the flux vector is used to approximate the (nonlinear) flux vector

$$\vec{F}(Q_i) \approx \boldsymbol{I}_k\left(\vec{F}(Q_i)\right) \equiv \sum_j L_j^{SP}(\vec{r})\vec{F}\left(Q_{i,j}\right) \tag{2.15}$$

where $L_j^{SP}(\vec{r})$ is the Lagrange polynomial based on the solution points $\{\vec{r}_{i,j}\}$. After that, the projection is computed using

$$\Pi\left(\nabla\cdot\vec{F}(Q_i)\right) = \nabla\cdot\boldsymbol{I}_k\left(\vec{F}(Q_i)\right) = \sum_j \nabla L_j^{SP}\cdot\vec{F}\left(Q_{i,j}\right) \tag{2.16}$$

In this case, $\Pi\left(\nabla\cdot\vec{F}(Q_i)\right)$ is a degree $k-1$ polynomial, which also belongs to P^k. Numerical experiments indicate that there is a slight loss of accuracy with the LP approach, but it is fully conservative [103].

We recognize that the divergence of the flux vector can be computed analytically given the approximate solution using the chain rule, i.e.,

$$\nabla\cdot\vec{F}\left(Q_{i,j}\right) = \frac{\partial F\left(Q_{i,j}\right)}{\partial x} + \frac{\partial G\left(Q_{i,j}\right)}{\partial x} = \frac{\partial F\left(Q_{i,j}\right)}{\partial Q}\frac{\partial Q_{i,j}}{\partial x} + \frac{\partial G\left(Q_{i,j}\right)}{\partial Q}\frac{\partial Q_{i,j}}{\partial y}$$

$$= \frac{\partial\vec{F}\left(Q_{i,j}\right)}{\partial Q}\cdot\nabla Q_{i,j} \tag{2.17}$$

where $\frac{\partial\vec{F}}{\partial Q}$ is composed of the flux Jacobian matrices, which can be computed analytically. Then projection is approximately by the Lagrange interpolation polynomial of the flux vector divergence at the solution points, i.e.,

$$\Pi\left(\nabla\cdot\vec{F}(Q_i)\right) \approx \sum_j L_j^{SP}(\vec{r})\,\nabla\cdot\vec{F}\left(Q_{i,j}\right) \tag{2.18}$$

Numerical experiments indicate that the CR approach is much more accurate than the LP approach, at the expense of full conservation [103].

Substituting Eq. (2.14) into Eq. (2.12) we obtain the following CPR formulation

$$\frac{\partial Q_{i,j}}{\partial t} + \Pi\left(\nabla \cdot \vec{F}\left(Q_i\right)\right) + \frac{1}{|V_i|}\sum_{f\in\partial V_i}\sum_{l}\alpha_{j,f,l}[F^n]_{f,l}S_f = 0 \qquad (2.19)$$

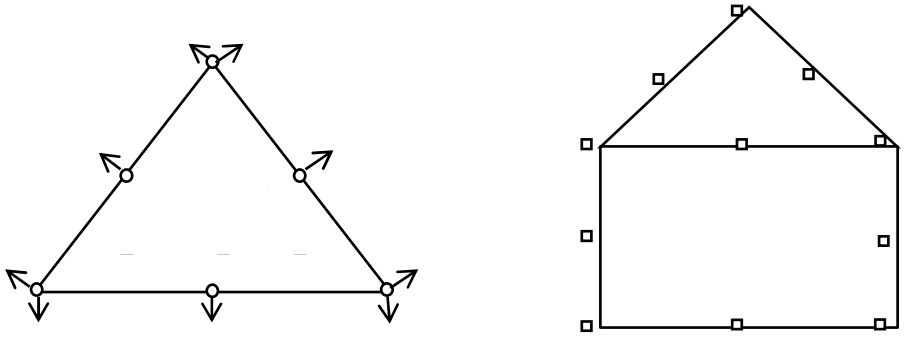

Figure 2.2. Efficient arrangement of solution (squares) and flux points (circles) for $k = 2$

It can be easily shown that the location of SPs does not affect the numerical scheme for linear conservation laws [90]. For efficiency, therefore, the solution points and flux points are always chosen to include corners of the cell. In addition, the solution points are chosen to coincide with the flux points along cell faces, as shown in Fig 2.2(a) to avoid any solution reconstruction. Furthermore, in computations with hybrid meshes, the flux points are always the same for different cell types for ease of interface treatment, as shown in Fig 2.2(b). For the 2D cases presented here, the Legendre-Lobatto points along the edges are used as the flux points for both triangular and quadrilateral cells. Due to special choice of DOFs, the reconstruction cost in CPR is completely avoided.

2.2 Treatment of Viscous Terms

2.2.1 Basic Framework

The discretization of viscous term in the DG method has been studied extensively in the literature [3,8,9,18,28,32,50,72,97]. The extension of the CPR formulation to viscous flows follows existing compact approaches developed in [9,18,50,72]. The Navier-Stokes equations can be written as

$$\frac{\partial Q}{\partial t} + \nabla \cdot \vec{F}(Q) = \nabla \cdot \vec{F}^{v}(Q, \nabla \mathrm{Q}) \tag{2.40}$$

where $\vec{F}^{v}(Q, \nabla \mathrm{Q})$ denotes the viscous flux vector.

First, following [8], we introduce a new variable $\vec{R}$

$$\vec{R} = \nabla Q \tag{2.41}$$

Let $\vec{R}_i$ be an approximation of $\vec{R}$ on V_i, and $\vec{R}_i \in (P^k, P^k)$. Many studies have found that the obvious choice of $\vec{R}_i = \nabla Q_i$ is not appropriate. Instead, the computation of $\vec{R}_i$ needs to involve data from neighboring cells. The CPR formulation of Eq. (2.40) and Eq. (2.41) on a linear triangle V_i can be expressed as

$$\frac{\partial Q_{i,j}}{\partial t} + \Pi_j \left(\nabla \cdot \vec{F}(Q_i)\right)$$

$$+\Pi_j^{v} \left(\nabla \cdot \vec{F}^{v}\left(Q_i, \vec{R}_i\right)\right) + \frac{1}{|V_i|} \sum_{f \in \partial V_i} \sum_{l} \alpha_{j,f,l} \left([F^n]_{f,l} - [F^{v,n}]_{f,l}\right) S_f = 0 \tag{2.42}$$

$$\vec{R}_{i,j} = (\nabla Q_i)_j + \frac{1}{|V_i|} \sum_{f \in \partial V_i} \sum_{l} \alpha_{j,f,l} [Q^{com} - Q_i]_{f,l} \vec{n}_f S_f \tag{2.43}$$

where Π^{v} is the projection operator for the divergence of the viscous flux vector to P^k, and

$$[F^{v,n}]_f \equiv \vec{F}^v\left(Q_f^{com}, \nabla Q_f^{com}\right) \cdot \vec{n}_f - \vec{F}^v\left(Q_i, \vec{\mathrm{R}}_i\right)\big|_f \cdot \vec{n}_f \tag{2.44}$$

with Q_f^{com} and ∇Q_f^{com} the common solution and gradient on interface f respectively, and Q_i, j, l is the solution within cell i on FP l of face f or the trace of Q_i on f. The computational of $\Pi_j^v\left(\nabla \cdot \vec{F}^v\left(Q_i, \vec{R}_i\right)\right)$ follows the LP approach. First, the viscous flux vector at each solution point is evaluated using

$$\vec{F}_{i,j}^v = \vec{F}^v\left(Q_{i,j}, \vec{R}_{i,j}\right) \tag{2.45}$$

After that, a Lagrange polynomial for the viscous flux vector is built with the values at all the solution points, i.e.,

$$\boldsymbol{I}_k\left(\vec{F}_i^v\right) = \sum_j \vec{F}_{i,j}^v L_j^{SP} \tag{2.46}$$

Finally the divergence of this polynomial is used as the projection

$$\Pi_j^v\left(\nabla \cdot \vec{F}^v\left(Q_i, \vec{R}_i\right)\right) \approx \nabla \cdot \boldsymbol{I}_k\left(\vec{F}_i^v\right) = \sum_j \vec{F}_{i,j}^v \cdot \nabla L_j^{SP} \tag{2.47}$$

Various schemes for viscous fluxes differ in how the common solution Q_f^{com} and the common gradient ∇Q_f^{com} are defined. It is sometimes to use a face based notation, in which $Q_f^- = Q_i$ and $Q_f^+ = Q_{i+}$.

2.2.2 Bassi-Rebay 1 (BR1)

In Bassi and Rebay original approach [9], the simple averages of the solution at both sides of the face were used for the numerical fluxes, i.e.,

$$Q_f^{com} = \frac{Q_f^- + Q_f^+}{2} \tag{2.48}$$

$$\nabla Q_f^{com} = \frac{\nabla Q_f^- + \nabla Q_f^+}{2} \tag{2.49}$$

2.2.3 Local Discontinuous Galerkin (LDG)

The idea of LDG [28] was proposed by Cockburn and Shu. The solution from one side of a face is used as the common solution, while the corrected gradient from the other side is used as the common gradient.

$$Q_{f,l}^{com} = Q_{f,l}^{+} \tag{2.50}$$

$$\nabla Q_{f,l}^{com} = \nabla Q_{f,l}^{-} \tag{2.51}$$

We also can alternately take the left and right limits for Q and ∇Q. In other words, $Q_{f,l}^{-}$ and $\nabla Q_{f,l}^{+}$ are taken as the common solution and common gradient.

The discretization of diffusive terms has been discussed by many researchers over the past decade. More compact and more accurate approaches were developed, which include the second Bassi and Rebay approach (BR2) [8], the I-continuous approach by Huynh [50], the interior penalty [33], and CDG [72]. In our study, only BR1 and LDG are considered, and LDG already provides good results.

CHAPTER 3. ONE-DIMENSIONAL FREQUENCY-OPTIMIZED CPR FORMULATION

In this chapter, the stability and accuracy of the CPR method for 1D linear problem is analyzed. Hybrid bases including both polynomial and Fourier bases are applied into the CPR method rather than the classic polynomial bases, with objective of resolving broad-band wave propagation problems. Free-parameters introduced by Fourier bases are optimized to minimize both the dispersion and dissipation errors by mimicking the DRP method [84, 85]. This method is named as frequency optimized CPR formulation (FOCPR). An analysis of the wave propagation properties of FOCPR is applied to assess both the stability and accuracy of the scheme. The mesh resolution analysis is applied to verify the optimization procedure by following the ideas [110]. Numerical tests are preformed to show that CPR scheme with optimized hybrid bases can resolve broad-band wave more accurately than that with the classic polynomial bases.

1D FOCPR is studied in this chapter, and the methodology is extended to 2D in the next chapter.

3.1 Framework of Wave Propagation Analysis

3.1.1 Basic Idea

The methodology of wave propagation analysis is introduced in this section. The approach is following the procedures by Hu [43] and Van den Abeele [86]. The simplest 1D conservation law that models wave propagation is used as the model problem. The 1D scalar

advection equation with periodic boundary conditions and a harmonic wave as initial solution is given as

$$\frac{\partial u}{\partial t} + a\frac{\partial u}{\partial x} = 0 \tag{3.1}$$

$$u(x,0) = e^{ikx} \tag{3.2}$$

where a is the positive wave speed. A Fourier wave of the form

$$u(x,t) = \hat{u}e^{I(kx-\omega t)+\vartheta_R t} \tag{3.3}$$

is introduced in this linear advection equation, which represents a sinusoidal wave train with a wave number k and an angular frequency ω. Eq. (3.3) is substituted into Eq. (3.1), and it is found that the following exact dispersion relation is

$$\vartheta_R = 0 \qquad \text{and} \qquad \omega = ak \tag{3.4}$$

ϑ_R is the dissipation rate, which determines the exponential growth or decay of the amplitude. Non-dimensional quantities are used in our analysis. The reference length scale for the non-dimensionalization is set as Δx and the time scale is $t = \frac{\Delta x}{a}$. The dimensionless parameters are expressed as

$$K = k\Delta x \tag{3.5}$$

$$\Omega = \omega\frac{\Delta x}{a} \tag{3.6}$$

where K and Ω are the non-dimension wave number and frequency, respectively. The exact dispersion relation is given as follows with non-dimensionalization.

$$\Omega = K \tag{3.7}$$

If the spatial derivative in the linear advection equation is discretized in space on a uniform grid with cell size Δx and the Fourier wave of the form Eq. (3.3) is applied in the discretization equation, then the resulting numerical solutions does not obey this exact dispersion relation any more, but a modified dispersion relation. This modified dispersion relation is close to the exact one, which is a measure for the accuracy of the spatial scheme. The modified dissipation rate should be non-positive, otherwise the solution will grow exponentially and thus divergence.

3.1.2 Extension to 1D CPR

To Eq. (3.1), a $(k+1)$ degree of freedom (DOFs) method will be applied on a uniform mesh Δx for CPR formulation, while classic finite difference methods have only one DOF. On a local coordinate $\xi \in [-1,1]$ for each element V_i. The approximate $Q_i = \sum_{j=1}^{P+1} W_j Q_{i,j}$ can be written as a function of ξ, and W_j is the shape function. On the boundaries between two elements, a Riemann is used as the common flux term.

$$F^R\left(u_i(1), u_{i+}(-1)\right) = a\left(\frac{1+\beta}{2}u_i(1) + \frac{1-\beta}{2}u_{i+}(-1)\right) \tag{3.8}$$

In (3.8), $\beta = 0$ corresponds to a central flux and $\beta = 1$ corresponds to the upwind flux. Upwind flux is applied in our work.

For 1D scalar advection equation on $\in [-1,1]$, the CPR scheme is reduces to the following matrix form

$$\frac{du_{i,m}}{dt} + \sum_{j=1}^{k+1} N_{mj}^{-1} u_{i-1,j} + \sum_{j=1}^{k+1} N_{mj}^{-1} u_{i-1,j} = 0, \qquad (m = 1, \cdots, k+1) \tag{3.9}$$

The matrix components N_{mj}^{-1} and N_{mj}^{0} are given in Appendix D.

Substitute of the expression of a Fourier wave $u(x,t) = \hat{u}e^{I(kx-\omega t)+\vartheta_R t}$ into Eq. (3.1), the numerical dispersion relation determined for upwind flux is given as

$$det\left(-I\Omega + e^{-IK}N^{-1} + N^{0}\right) = 0 \tag{3.10}$$

Eq. (3.10) has $k+1$ solution, corresponding to the $k+1$ eigenmodes of the numerical system. The quantity $-I\Omega$ is called Fourier footprint and $\mathcal{R} = \mathcal{R}^{\mathrm{Re}} + i\mathcal{R}^{\mathrm{Im}}$, and the imaginary part $\mathcal{R}^{\mathrm{Im}}$ is a measure of dispersive properties of the scheme, whereas the real part $\mathcal{R}^{\mathrm{Re}}$ represents the diffusive behavior which should be non-positive to keep the scheme stable.

Note that a CPR scheme is using a polynomial approximation of degree k, wave with non-dimensional wave numbers K ranging from $-(k+1)\pi < K < (k+1)\pi$ are captured, since there are $k+1$ degrees of freedom per element. For classic FV method, the wave range is $-\pi < K < \pi$, which corresponds to the one degree of freedom per element by such methods. To make a fair comparison between the FV and the different order CPR schemes, the plot for the CPR method should be downscaled with a factor $k+1$, taking into account the higher number of degrees of freedom of CPR.

The diffusive and dispersive properties are then plotted versus the wave number in Fig 3.1by using the 4$^{\text{th}}$ order piecewise polynomial bases as local spaces in CPR methods with uniform solution point distribution. Fig 3.1 shows $\mathcal{R}^{\mathrm{Re}}$ and $\mathcal{R}^{\mathrm{Im}}$ for the fourth-order CPR scheme ($k=3$), when an upwind Riemann flux is used. For this scheme, K ranges from -4π to 4π. When $\mathcal{R}^{\mathrm{Re}}$ and $\mathcal{R}^{\mathrm{Im}}$ are plotted versus the dimensionless wave number K, there are $k+1$ values for each K, which correspond to the $k+1$ eigenvalues of equation (3.10). The eigenvalue solution shapes should be examined to identify the physical ones. From Fig

3.1 of the mode shapes, the actual wave number to which a certain eigenvalue belongs can easily be determined.

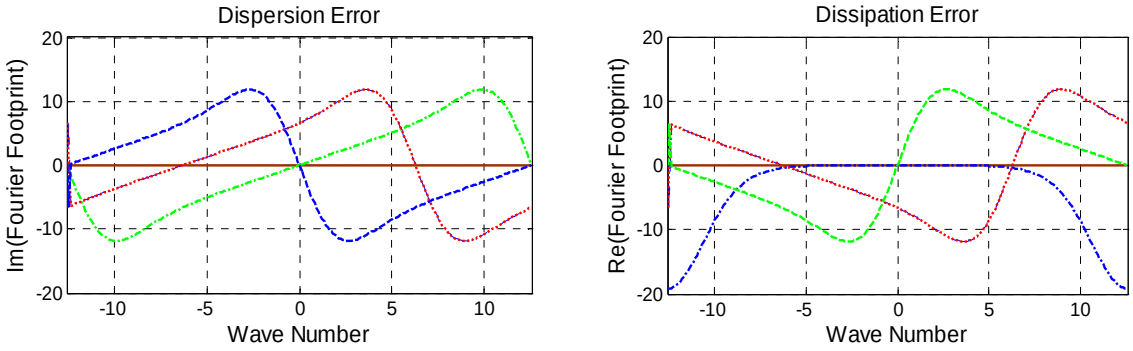

Figure 3.1. Eigenvalues of the 4th order CPR schemes ($\boldsymbol{\mathcal{R}}^{\mathbf{Re}}$ and $\boldsymbol{\mathcal{R}}^{\mathrm{Im}}$ versus $\boldsymbol{K}$)

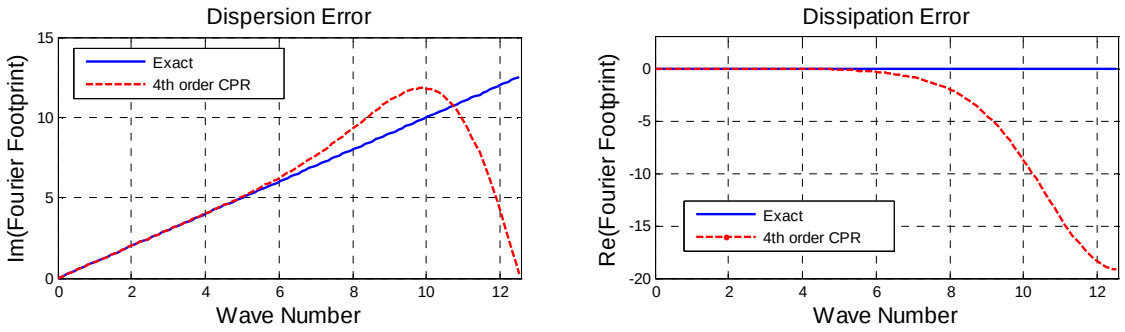

Figure 3.2. Diffusion error and dissipation error of the 4th order CPR schemes

($\mathcal{R}^{\mathrm{Re}}$ and $\mathcal{R}^{\mathrm{Im}}$ versus K)

In Fig 3.2, the curves are only shown for positive K due to the symmetry. It is clear that the scheme is stable, because the dissipation errors $\mathcal{R}^{\mathrm{Re}}$ is always non-positive. Notice that the scheme becomes less accurate for increasing wave numbers. The present 4th order CPR scheme with a piece-wise polynomial as bases has good wave propagation properties for dimensionless wave number up to $K \approx 5$.

3.2 Hybrid Bases Including Both Polynomial and Fourier Bases

The piecewise polynomial space is the common chosen approximation space, when discontinuous high-order method is used to solve partial differential equations (PDEs). However for some PDEs and initial/boundary conditions, piecewise polynomials may not provide the best approximation to the solutions, such as the boundary layer and highly oscillatory problems. The approximation spaces can be different with respect to each element and also to different time t, so the local approximation spaces can be any linear spaces.

Cockburn [30] et al. proposed the use of the locally divergence-free polynomial space to resolve the Maxwell equations and achieved better results compared with the classical piecewise polynomial bases in DG method. The singular perturbation problems are solved by using exponentially fitted schemes by of Kadalbajoo and Patidar [52], and Reddy and Chakravarthy [73]. Christofi [20] used non-polynomial spaces in local essentially non-oscillatory (ENO) reconstructions for solving hyperbolic conservation laws. The DG method bases on exponential functions and trigonometric functions is studied in [109] in order to obtain better approximation for specific types of PDEs and initial/boundary conditions. For the boundary layer problems, the slope of the solution near the boundary is very large, exponential functions achieved better results than the classic polynomial functions. For the highly oscillatory problems, the solution is better approximated by trigonometric functions.

In our proposed method, hybrid bases including both polynomial and Fourier bases are developed to resolve broad-band wave propagation problems, rather than the classical polynomial bases. Polynomial bases, Fourier bases and hybrid bases are defined as follows, respectively.

$$T \in span(1, x, x^2, x^3 \cdots) \tag{3.11}$$

$$T \in span(sin(\alpha 1 * x), cos(\alpha 1 * x), sin(\alpha 2 * x), cos(\alpha 2 * x) \cdots) \quad (3.12)$$

$$T \in span(1, x, x^2, x^3 \cdots, sin(\alpha 1 * x), cos(\alpha 1 * x), sin(\alpha 2 * x), cos(\alpha 2 * x) \cdots) \quad (3.13)$$

$(\alpha 1, \alpha 2, \cdots)$ are Free-parameters. The Fourier bases are applied here in order to resolve a relatively large wave number for a wave propagation problem, while the polynomial bases are applied here in order to keep a certain order of accuracy.

Due to Fourier spaces, the exact dispersion relation $\Omega = K$ is exactly satisfied at a certain K. For example if the base $T = \left(1, x, sin(2 * x), cos(2 * x)\right)$ is applied, the analytical physical dimensionless dispersion relation should be $\Omega = K = k * \Delta x = 2 * 2 = 4$. This means that the dispersion errors $(\mathcal{R}^{Re} - K)$and dissipation errors $\mathcal{R}^{Im}$ should equal to zero at non-dimensional wave number 4.

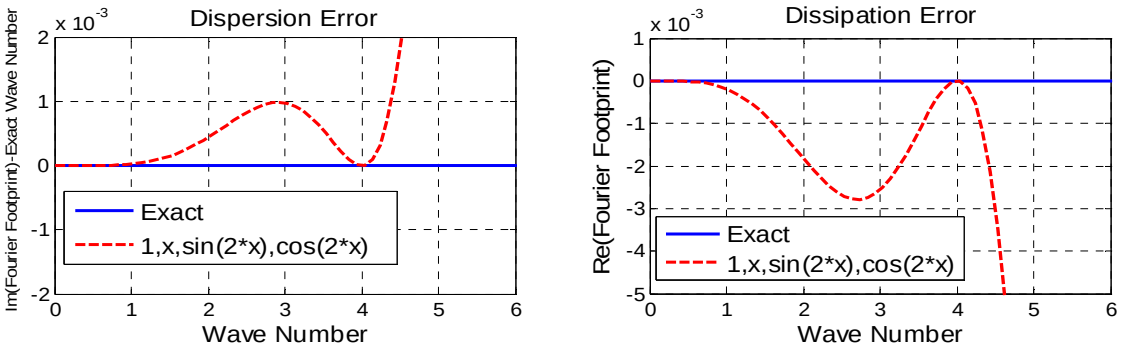

Figure 3.3. Dispersion errors $(\mathcal{R}^{Re} - K)$ and Dissipation errors $\mathcal{R}^{Im}$ versus K for $T = \left(1, x, sin(2 * x), cos(2 * x)\right)$

In Fig 3.3, both dispersion errors $(\mathcal{R}^{Re} - K)$ and dissipation $\mathcal{R}^{Im}$ are plotted with hybrid bases $T = \left(1, x, sin(2 * x), cos(2 * x)\right)$. It shows that dispersion and dissipation errors are equal to zero at non-dimensional wave number 4. Uniform point distribution is used in this case. Due to this specific property, we can design CPR schemes with specific hybrid bases to exact simulate a wave equation with certain non-dimensional wave numbers.

3.3 Optimization of Hybrid Bases

In this section, free-parameters in the hybrid bases are optimized to minimize both dispersion and dissipation errors by mimicking the similar idea of dispersion-relation-preservation (DRP) [84, 85]. The wave propagation characteristics are encoded in the dispersion relations of the governing equations according to wave propagation analysis. It is expected that the numerical solutions of high-order formulations will have the same wave propagation characteristics as those of the solutions of the governing equations if both systems of equations have the same dispersion relation. So minimum numerical dispersions and dissipations are required to get an accurate amplitude and phase for numerical calculation of wave propagation [84, 85]. The optimized schemes such as the central DRP [84, 85] and the upwind DRP [111, 112] schemes are to assure the transform of the scheme be a good approximation of that the partial derivative over a certain range of wave number.

3.3.1 Dispersion-Relation-Preservation (DRP) Method

The main idea of DRP schemes is to optimize high order finite difference scheme not only meets the usual conditions of consistency, stability and convergence, but also has the same or almost dispersion relation as the original partial differential equations. As we know that the dispersion relation is a functional relation between the angular frequencies of the wave and the wave numbers of the spatial variables.

In developing finite difference approximation of partial derivatives, the standard way is to use a truncated Taylor series. But from the wave propagation point of view, the motivation is to preserve the dispersion relation, so the finite difference approximation should be constructed so that the Fourier transform is preserved. In other words, it would be desirable

to have a finite difference scheme with nearly the same Fourier transform in space or time as the original partial derivative. The DRP methodology is given here briefly.

The approximation of the first-order spatial derivative $\frac{\partial u}{\partial x}$ on uniform grids for a finite difference method is given by

$$\left(\frac{\partial u}{\partial x}\right)_i \approx \frac{1}{\Delta x}\sum_{j=N}^{M} a_j u(x_i + j\Delta x) \tag{3.14}$$

where M values of f to the right and N values of f to the left of this point. The finite difference methods will be referred as the standard schemes if the coefficients a_j are determined by equating coefficients of the same powers of Δx with Taylor expansion series. For DRP method, the coefficients a_j are to be chosen in a different way. The basic idea of DRP is that the coefficients are determined by requiring the Fourier transform of the finite difference scheme on the right of (3.14) to be a close approximation of the partial derivative on the left. The finite difference equation (3.14) is a special case of the following equation in which x is a continuous variable:

$$\frac{\partial u}{\partial x}(x) \approx \frac{1}{\Delta x}\sum_{j=N}^{M} a_j u(x + j\Delta x) \tag{3.15}$$

The Fourier transform and its inverse of a function are related by

$$\tilde{u}(\alpha) = \frac{1}{2\pi}\int_{-\infty}^{\infty} u(x)e^{-i\alpha x}dx \tag{3.16}$$

$$u(x) = \frac{1}{2\pi}\int_{-\infty}^{\infty} \tilde{u}(\alpha)e^{i\alpha x}d\alpha \tag{3.17}$$

The Fourier transform of the both sides of (3.18) is

$$i\alpha\tilde{u} \approx \left(\frac{1}{\Delta x}\sum_{j=-N}^{M} a_j e^{i\alpha j\Delta x}\right)\tilde{u} \tag{3.18}$$

By comparing the both side of equation (3.21) to get the following equation

$$\bar{\alpha} = \frac{-i}{\Delta x}\sum_{j=-N}^{M} a_j e^{i\alpha j\Delta x} \tag{3.19}$$

The left side is the effective wave number and $\bar{\alpha}\Delta x$ is a function of $\alpha\Delta x$ with the period 2π. a_j were chosen to minimize the integrated error E defined in (3.20) in order to assure that the Fourier transform of the finite difference scheme is a good approximation of the partial derivative over the range of wave numbers of interest.

$$E = \int_{-\pi/2}^{\pi/2} |\alpha\Delta x - \bar{\alpha}\Delta x|^2 \, d(\alpha\Delta x) = \int_{-\pi/2}^{\pi/2} \left| iK - \sum_{j=-N}^{M} a_j e^{ijK} \right|^2 dK \tag{3.20}$$

The condition that E is a minimum are

$$\frac{\partial E}{\partial a_j} = 0, \quad j = -N \; to \; M \tag{3.21}$$

(3.21) provides a system of linear algebraic equations by which the coefficients a_j can be easily determined.

3.3.2 Optimization of Free-Parameters of Hybrid Bases

Free-parameters in the hybrid bases for the CPR method are optimized by mimicking the similar idea of DRP [84, 85] to maximize the resolvable wave number given a certain error threshold. The following two conditions are applied.

- The optimization process has to allow the normalized value of $\Omega_{\mathrm{Im}}/N - K/N$ and Ω_{Re}/N to be as close to zero as possible for certain integration wave numbers. N is the order of DOFs.

$$E = \int_0^e |\Omega_{\mathrm{Im}}/N - K/N|^2 dK + \lambda \int_0^e |\Omega_{\mathrm{Re}}/N|^2 dK \tag{3.22}$$

The weight λ is set as 0.2 to balance the L_2 norm of the truncated errors of dispersion and dissipation. e is a predetermined optimized range of wave numbers.

- In order to quantify the resolution of the scheme, set the dispersion and dissipation errors to less than 0.5%, i.e.[43]

$$|\Omega_{\mathrm{Im}} - \mathrm{K}| < 0.005 \qquad \text{and} \qquad |\Omega_{\mathrm{Re}}| < 0.005 \tag{3.23}$$

Table 3.1. Optimization free-parameter **α** of Fourier bases

for $\boldsymbol{T = (1, x, sin(\alpha x), cos(\alpha x))}$

Integration range (e)	α	E - Dispersion	E-diffusion	E
$\pi \approx 3.14$	1.4	$2.1477e-09$	$2.7483e-08$	$7.6444e-09$
$5 * \pi/4 \approx 3.93$	1.7	$1.6503e-07$	$1.0139e-06$	$3.6781e-07$
$3 * \pi/2 \approx 4.71$	2.1	$3.8702e-06$	$2.4832e-05$	$8.8367e-06$
$7 * \pi/4 \approx 5.50$	2.4	$6.1540e-05$	$2.6556e-04$	$1.1465e-04$
$2 * \pi \approx 6.28$	2.7	$6.5403e-04$	$2.1424e-03$	$1.0825e-03$

Table 3.2. Maximum resolvable wave number K_c

For $T = (1, x, sin(\alpha x), cos(\alpha x))$

Integration range	α	K_c
$\pi \approx 3.14$	1.4	3.9336
$5 * \pi/4 \approx 3.93$	1.7	4.2336
$3 * \pi/2 \approx 4.71$	2.1	4.8336
$7 * \pi/4 \approx 5.50$	2.4	2.0336
$2 * \pi \approx 6.28$	2.7	1.6336

In Table 3.1, hybrid bases $(1, x, sin(\alpha * x), cos(\alpha * x))$ are applied in CPR method with fourth degree of freedom. E-dispersion represents the dispersion integration errors, and E-dissipation means the dispersion integration errors. E represents the dispersion errors plus $0.2 *$ dissipation errors, which are defined in Eq. (3.22). Free-parameters α in Table 3.1 are found to minimize the integration error E through numerical searches for a certain wave number integration range e. In other words, the CPR schemes with α shown in Table 3.1 obtain the minimum dispersion errors with respect to different range e.

In Table 3.2, the maximum resolvable non-dimensional wave numbers K_c are determined using Eq. (3.23) for each α with respect to a certain integration wave number e. This means when the non-dimensional wave numbers are smaller than K_c, Eq. (3.23) is satisfied. In other words, when the non-dimensional wave number is greater than K_c, the dispersion and dissipation errors are greater than 0.5%. So K_c is called the maximum resolvable non-dimensional wave number.

From Table 3.2, we can see that K_c increases and then decreases as the integration range e increases. $\alpha = 2.1$ is referred as the optimized free-parameter, which minimizes the integration error E over a relatively large wave number integration range 4.71, and at the same time the resolvable wave number K_c reaches 4.83, with which both dispersion and dissipation errors are less than 0.5% defined in Eq. (3.23). In other words, the maximum resolvable non-dimensional wave number K_c is equal to 4.83 corresponding to the integration range $e = 3 * \pi/2$, and $\alpha = 2.1$ gives smallest dispersion errors.

The same procedure is applied for the higher DOFs scheme. $\alpha = 4.0$ is the optimized free-parameter with the integration wave number range 8.60 for $\left(1, x, x2, x3, sin(\alpha * x), cos(\alpha * x)\right)$, and $\alpha 1 = 4.5$ and $\alpha 2 = 3.0$ are the optimized free-parameters with the integration wave number 9.42 for $\left(1, x, sin(\alpha 1 * x), cos(\alpha 1 * x), sin(\alpha 2 * x), cos(\alpha 2 * x)\right)$ with the dispersion and dissipation errors to less than 0.5%.

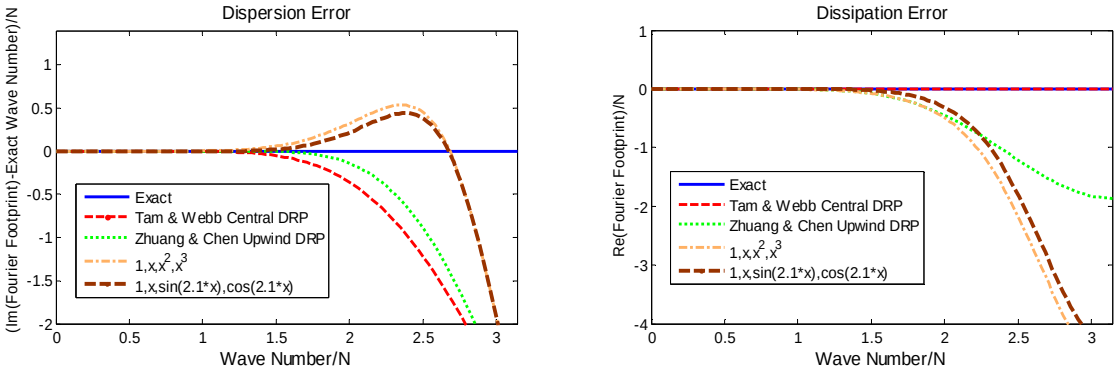

Figure 3.4. Comparison of normalized dispersion errors $(\mathcal{R}_{\mathrm{Im}} - \mathrm{K})/\mathrm{N}$ and normalized dissipation errors $\mathcal{R}_{\mathrm{Re}}/N$ versus K/N for 4 DOFs for 4 DOFs hybrid bases

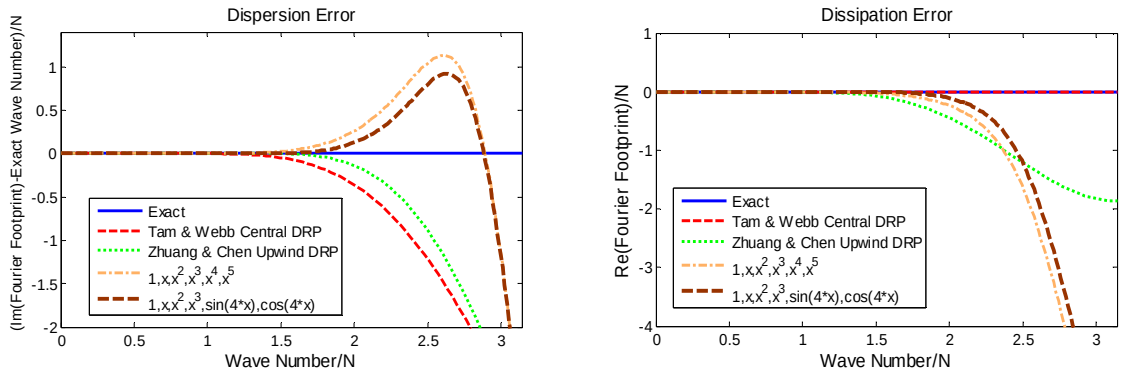

Figure 3.5. Comparison of normalized dispersion errors $(\mathcal{R}_{Im} - K)/N$ and normalized dissipation errors $\mathcal{R}_{\mathrm{Re}}/N$ versus K/N for 6 DOFs for 4 DOFs hybrid bases

The upwind CPR schemes with the optimized hybrid bases are compared with the corresponding polynomial bases, Tam & Webb's central DRP and Zhuang & Chen DRP in terms of dispersion and dissipation errors. In order to compare different DOFs schemes, normalized values are applied here. For high-order CPR schemes, uniform point distribution is used.

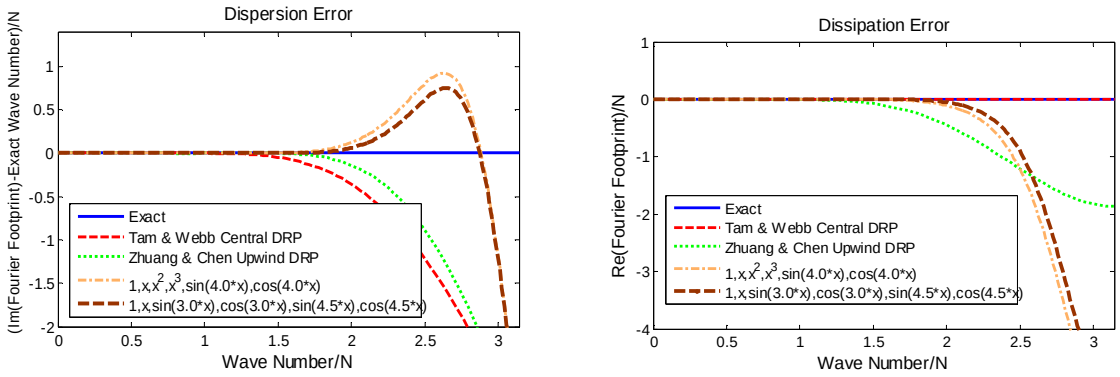

Figure 3.6. Comparison of normalized dispersion errors $(\mathcal{R}_{Im} - K)/N$ and normalized dissipation errors $\mathcal{R}_{\mathrm{Re}}/N$ versus K/N for 6 DOFs hybrid bases with more Fourier terms

In Fig 3.4, the upwind CPR formulation with the optimized hybrid bases $T = \left(1, x, sin(2.1 * x), cos(2.1 * x)\right)$ is compared with the corresponding formulations. The normalized dispersion errors and dissipation errors are plotted versus normalized non-dimensional wave numbers. The optimization scheme shows less dispersion errors than the polynomial base and the Tam & Webb's central DRP scheme, but a little bit larger dispersion errors than Zhuang & Chen's upwind DRP scheme. It is able to resolve the waves with non-dimensional wave numbers as high as about 1.3 which is very close to the seven stencil finite difference schemes, although it is a four stencil scheme.

In Fig 3.5, the optimized six stencil scheme $\left(1, x, x2, x3, sin(4.0 * x), cos(4.0 * x)\right)$ has obviously less dispersion and dissipation errors than the corresponding polynomial bases,

central DRP and upwind DRP. And it is able to resolve the waves with non-dimensional wave number as high as about 1.6.

In Fig 3.6, the optimized six stencil scheme $(1, x, sin(3.0 * x), cos(3.0 * x), sin(4.5 * x), cos(4.5 * x))$ has less dispersion and dissipation errors than those of $(1, x, x2, x3, sin(4.0 * x), cos(4.0 * x))$. And it is able to resolve the waves with non-dimensional wave number as high as about 1.8. From all above analysis, the higher orders the schemes are and the more Fourier terms are used, the less dispersion and dissipation errors there are.

3.4 Mesh Resolution Analysis

In this section, the mesh resolution analysis is applied here to verify the optimization procedure by following the ideas [51, 110]. The number of grid points per wavelength (PPW) is presented, with objective of accurately simulating wave propagation over large distance. As we know that numerical errors arise from both the spatial and the temporal discretization. They include both phase and amplitude errors, which depend on the wave numbers, the grid spacing, the Courant number, and the direction of propagation relative to the grid. The dependence of the phase speed on the wave numbers results in numerical dispersion. This section presents the grid resolution required to achieve a specific level of accuracy as a function of the propagation distance expressed in terms of the wavelength for the previous optimized hybrid bases. Emphasis is on methods requiring under 60 grid points per wavelength (PPW) for accurate simulations with propagation distances of 200 wavelengths. The purpose is to aid in verifying the optimization procedure for the CPR method with hybrid bases. Here we only consider the accuracy of the interior CPR scheme without

considering boundary conditions. For the analysis, only the standard one order time discretization is used as time marching methods.

The mesh resolution analysis is also based on Fourier analysis in the absence of boundary conditions. In one dimension, the errors produced by the numerical formulations are function of the non – dimensional wave number K and the courant number $C = ah/\Delta x$. In multi – dimensions, the errors depend on the direction of propagation relative to the grid. The mesh resolution analysis is based on the amplification factor $\sigma(K, C) = u_{m+1}/u_m$, where m is the current time step and $m + 1$ is the next time step. PPW is the points per wave length and PPW $= \frac{\text{wavelength}}{\Delta x} = 2\pi/(k\Delta x)$.

The local amplitude and phase errors are, respectively

$$Error_a = |\sigma| - 1 \tag{3.24}$$

$$Error_p = -\frac{\phi}{KC} - 1 \tag{3.25}$$

Where $\phi = tan^{-1}(\sigma_{\text{Im}}/\sigma_{\text{Re}})$, and σ_{Im} and σ_{Re} are the real and imaginary part of σ, respectively. Criterion for comparing schemes is based on the global amplitude and phase errors which are

$$Error_a = \left||\sigma|^{PPW*n/C} - 1\right| < 10\% \tag{3.26}$$

$$Error_p = n * \left|\frac{PPW * \phi}{C} + 2\pi\right| < 10\% \tag{3.27}$$

Where n is the number of the wavelength travelled. Using the above formulas with a very small Courant number gives the errors for the spatial operator alone. In the following figures, the various methods are compared in terms of the PPW required to keep both global

amplitude and phase errors less than 10% as a function of the number of wavelength traveled.

In this section, we only consider the errors produced by the spatial operators. The error from a spatial discretization is often plotted in terms of the non-dimensional wavenumber. Plots of the local phase and amplitude errors can be much more revealing and provide a stronger physical connection. The global errors are even easier to interpret. In studying the dependence of the PPW requirements on the number of wavelengths travelled, the emphasis is on the wavenumber present in the simulation which is most poorly resolved among those wavenumbers which are deemed to be significant. The dependence of the PPW requirements on the number of wavelengths is a reasonable measure for selecting a grid density and reveals the implications of optimization. In this section, only spatial operators are considered by setting Courant numbers small enough.

In Fig 3.7, point per wavelength (PPW) requirement are presented for upwind CPR with respect to $(1, x, sin(\alpha * x), cos(\alpha * x))$. $\alpha = 2$ is superior up to a distance of travel about 45 wavelengths based on 10% global phase error criterion and about 15 wavelengths based on 10% global amplitude error criterion and requires about less than 5.0 PPW. Such behavior is typical of optimized schemes. Usually aggressive optimization leads to excellent performance for small distances of travel but poor performance for longer distances. This property agrees with the previous analysis that the optimized free-parameter $\alpha = 2.1$, which is close to 2, shows good dispersion and dissipation properties with the relatively large wave number given a certain resolution error criterion. In Fig 3.8, the PPW requirements for upwind CPR schemes with $(1, x, x^2, x^4, sin(\alpha * x), cos(\alpha * x))$ are presented. $\alpha = 4$ shows typical optimization behavior which requires about 4.5 PPW for about 40 wavelength travel

distance based on 10% phase error criterion and which requires about 4.5 PPW for about 25 wavelength travel distance based on 10% amplitude error criterion.

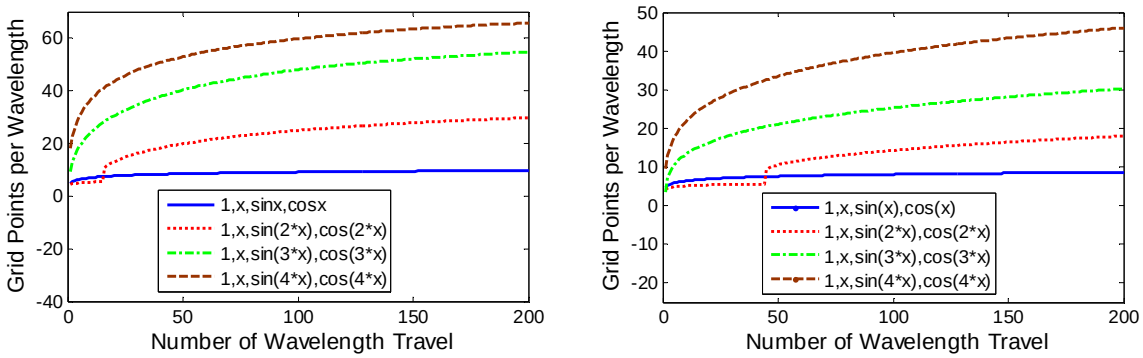

Figure 3.7. Grid resolution requirements based on globe amplitude and phase errors for hybrid bases $\left(1, x, sin(\alpha * x), cos(\alpha * x)\right)$

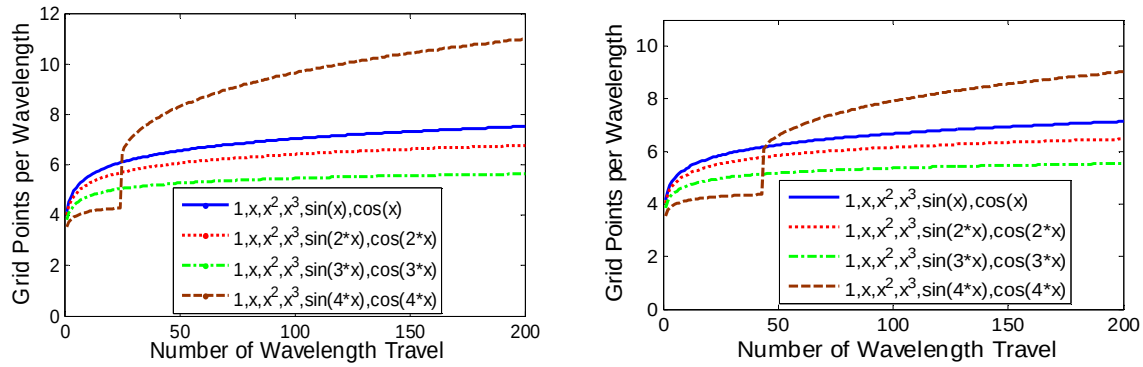

Figure 3.8. Grid resolution requirements based on globe amplitude and phase errors for hybrid bases $\left(1, x, x^2, x^4, sin(\alpha * x), cos(\alpha * x)\right)$

In Fig 3.9, the PPW requirements for CPR schemes with $\left(1, x, sin(\alpha 1 * x), cos(\alpha 1 * x), sin(\alpha 2 * x), cos(\alpha 2 * x)\right)$ are presented. $\alpha 1 = 3.0$ and $\alpha 2 = 4.0$ shows the typical optimization behavior too and the propagation distance is short, that requires about 4.0 PPW

for about 125 wavelength travel distance base on 10% phase error criterion and require about 5.0 PPW for about 40 wavelength travel distance based on 10% amplitude error criterion.

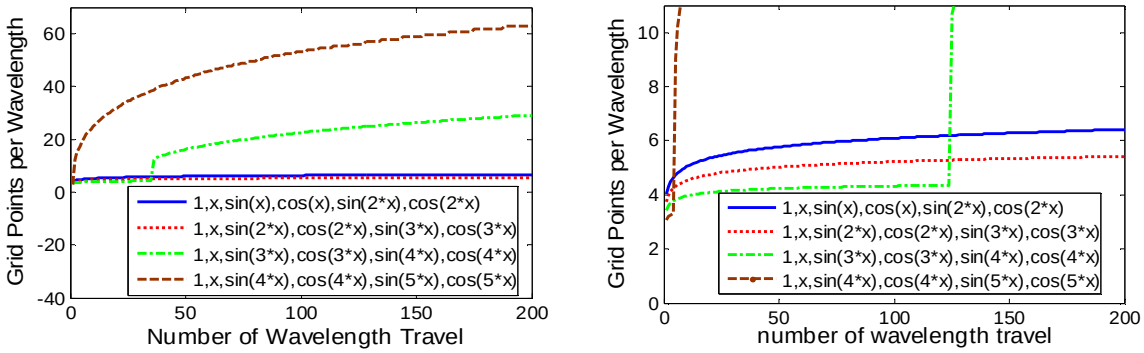

Figure 3.9. Grid resolution requirements based on globe amplitude and phase errors for hybrid bases $(1, x, sin(\alpha 1 * x), cos(\alpha 1 * x), sin(\alpha 2 * x), cos(\alpha 2 * x))$

The PPW analysis matches the optimization analysis perfectly, and both methods can be used to verify each other. More Fourier terms there are, the fewer PPW are required. For optimized schemes, when the degree of freedom increases, not only does fewer PPW require, but also the propagation distance is longer. Because the optimized schemes are optimized for a given range of wave number, they required fewer PPW if the propagation distance is relative short. As the number of wavelength traveled increase, the advantage of the optimized schemes diminished as the required PPW increase. However if fewer PPW is required, the use of optimized scheme not only gives most accurate results but also results in significant saving of CPU time.

3.5 Numerical Tests

3.5.1 Exact Solution for 1D Wave Equation with Sine Wave as an Initial Condition

According to previous Fourier analysis, the exact dispersion relation $\Omega = K$ is exactly satisfied at a certain K because of Fourier bases in hybrid bases. This problem is designed to verify the performance of the wave propagation characteristics of CPR formulation. The 4th order DOFs hybrid bases $(1, x, sin(\alpha x), cos(\alpha x))$ are applied here and 1D convective wave equation is considered.

$$\frac{\partial u}{\partial t} + a\frac{\partial u}{\partial x} = 0 \quad (a = 1) \tag{3.28}$$

On the uniform mesh with the initial condition is given as follows

$$u(x, 0) = sin(\pi * x) \tag{3.29}$$

π is the physical wave number for this initial condition. The procedures designed to catch the initial physical wave number are given as follows.

- First set grid size is equal to Δx, and calculate the non-dimensional wave number in the initial condition in Eq. (3.29).

$$K_1 = k * \Delta x = \pi * \Delta x \tag{3.30}$$

where the non-dimensional wave number is equal to the value (the physical wave number times the grid size).

- Choose a 4th order DOFs hybrid base $(1, x, sin(\alpha * x), cos(\alpha * x))$ and calculate the non-dimensional wave number on the standard computational domain related to the hybrid bases.

$$K_2 = \alpha * \Delta\xi \quad and \quad \Delta\xi = 2 \xrightarrow{yields} K_2 = 2 * \alpha \tag{3.31}$$

- Finally set these two non-dimensional wave numbers equal to each other to get the parameters in the hybrid bases

$$K_1 = K_2 \xrightarrow{yields} \alpha = (\pi * \Delta x)/2 \tag{3.32}$$

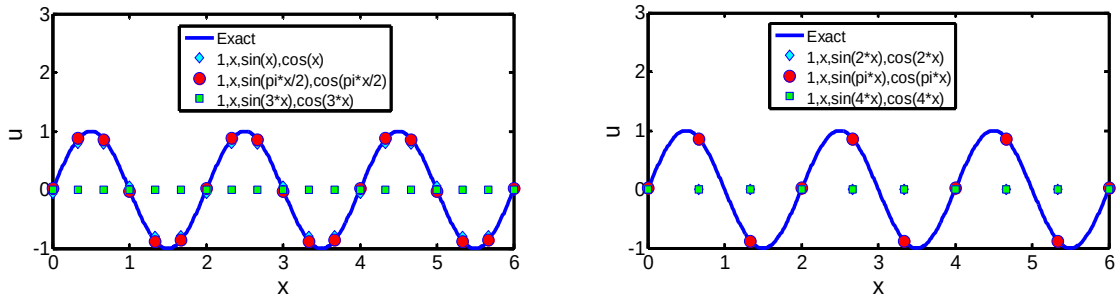

(a) (b)

Figure 3.10. Exact solution for 1D wave equation with sine wave as an initial condition

$\Delta t = 0.01, T = 60$, (a) $\alpha = (\pi * \Delta x)/\Delta\xi = \frac{\pi}{2}, \Delta x = 1$, (b) $\alpha = (\pi * \Delta x)/\Delta\xi = \pi, \ \Delta x = 2$

Fig 3.10 shows that the designed spaces exactly numerically simulate the wave equations (3.28) with the initial condition (3.29). (a) The space $\left(1, x, sin\left((\pi * x)/2\right), cos\left((\pi * x)/2\right)\right)$ is exactly simulating the wave equation when $\Delta x = 1$ (b) The space $(1, x, sin(\pi * x), cos\pi * x)$ is exactly simulating the wave equation when $\Delta x = 2$.

3.5.2 A Benchmark Problem-CAA Workshop (2004)

A benchmark problem is applied here to verify some properties of the bases. The governing equation is the scalar wave equation with unit wave speed as defined as equation (3.28) with the following initial condition

$$u(x, 0) = [2 + cos(\beta * x)]exp[-ln2(x/10)^2], \ \beta = 1.7 \ or \ 4.6 \tag{3.33}$$

Two different frequencies $\beta = 1.7$ and $\beta = 4.6$ are considered, and set $\Delta x = 1$ for an equivalent 1 DOF. At this grid resolution, the high frequency wave embedded in the initial condition only has about 3.7 and 1.9 points-per-wave (PPW). It is therefore a challenge for any numerical scheme to adequately resolve the high frequency wave.

The hybrid bases including Fourier bases which can resolve broadband wave propagation problems are applied in order to get more accurate results in this challenge situation. In order to get a better simulation for this problem, firstly find the approximation space $\big(1, x, sin(\alpha * x), cos(\alpha * x)\big)$, which can exactly simulation the initial high frequency wave condition $cos(\beta * x)$, then apply this approximation space for the wave equation with the initial condition of Eq. (3.33).

For the case $\beta = 1.7$, if we set $\Delta x = 3$ and follow the procedures described in the last section to get $a = 2.55$ for the 4th DOFs hybrid bases $\big(1, x, sin(\alpha * x), cos(\alpha * x)\big)$. It is expected that the hybrid bases with $a = 2.55$ can exactly simulate the wave equation with the initial condition $cos(\beta * x)$. The time integration was carried out using a fourth-order four stage Runge-Kutta scheme. A constant time step 0.05 was used for all cases.

In Fig 3.11, the numerical results of spaces $(1, x, x^2, x^3)$,$\big(1, x, sin(2.55 * x), cos(2.55 * x)\big)$ and $\big(1, x, sin(4.0 * x), cos(4.0 * x)\big)$ are presented. It is obvious that $a = 2.55$ show much less dissipative behavior. This confirms our expectation.

In Fig 3.12, the solutions of the upwind CPR scheme with the optimized approximation space 6th DOFs $\big(1, x, x^2, x^3, sin(4.0 * x), cos(4.0 * x)\big)and\big(1, x, sin(3.0 * x), cos(3.0 * x), sin(4.5 * x), cos(4.5 * x)\big)$ are compared with the 6th order polynomial approximation space for initial conditions for both $\beta = 1.7\ and\ 4.6$ with $T = 500S$ and $\Delta x = 5$. Both

hybrid bases show better simulations than the polynomial approximation space. It is clear that the more Fourier bases there are, the more accurate the results are. All of results agree with our expectation.

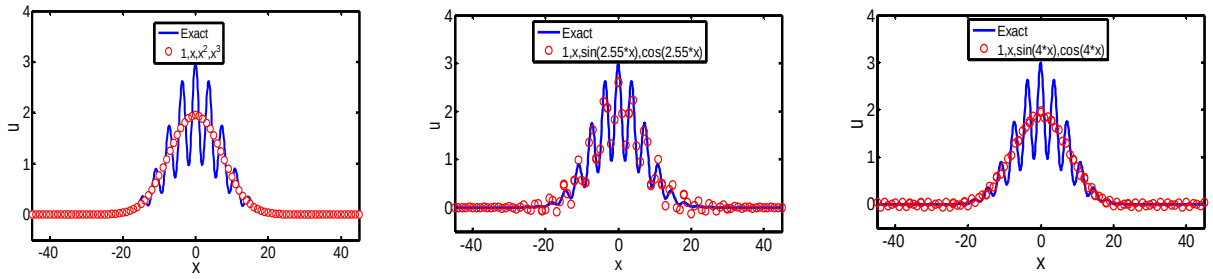

Figure 3.11. Numerical solution of 1D wave equation with the initial condition (3.33) for $\beta = 1.7$ ($T = 450S$ and $\Delta x = 3$, 4 DOFs upwind CPR scheme)

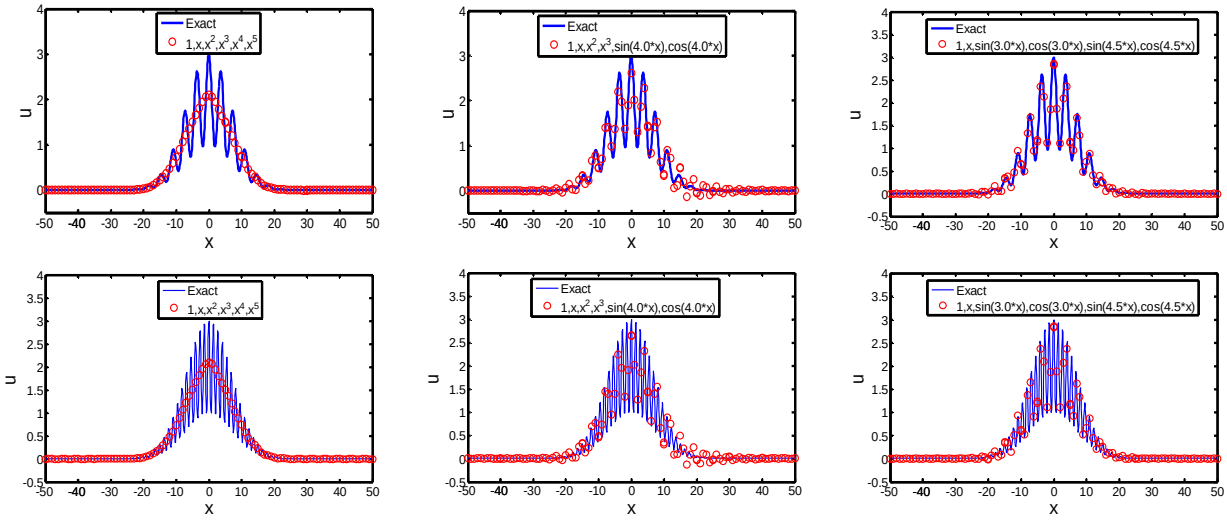

Figure 3.12. Numerical solution of 1D wave equation with the initial condition (3.33) ($T = 500S$ and $\Delta x = 5$, 6th DOF upwind) and first row $\beta = 1.7$ and second row $\beta = 4.6$

3.5.3 An Artificial "Broadband" Wave

The upwind CPR schemes are tested for an artificial "broadband" wave, which is The upwind CPR schemes are tested for an artificial "broadband" wave, which is followed the same procedure in [99]. The composed three waves are given as following

$$u_0(x) = sin(\pi * x/3) + sin(\pi * x/6) + sin(\pi * x/12) \tag{3.34}$$

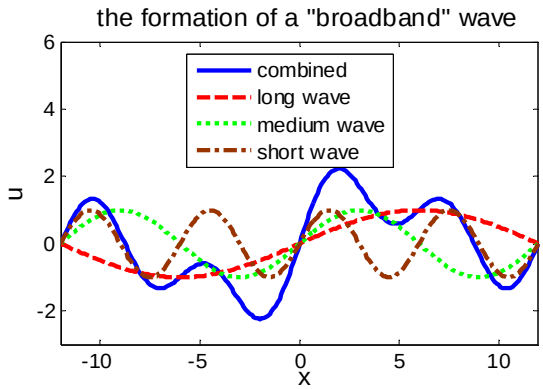

Figure 3.13. The formation of a "broadband" wave

The three waves represent short, medium and long waves and the wavelengths are 6, 12 and 24 respectively. The initial form is displayed in Fig 3.13. The computational domain is chosen to be $[-12, 12]$ and $\Delta t = 0.1S$ and $T = 24S$.

In Fig 3.14, the numerical results of the upwind CPR are compared with respect to bases $(1, x, x^2, x^3, x^4, x^5)$, and $\left(1, x, x^2, x^3, sin(4.0 * x), cos(4.0 * x)\right)$ for $\Delta x = 6.0$. Points-per-wavelength (PPW) is equal to 6.0 for the short wave. According to mesh resolution analysis, PPW requirement for $\left(1, x, x^2, x^3, sin(4.0 * x), cos(4.0 * x)\right)$ is about 4.5 and PPW requirement for $(1, x, x^2, x^3, x^4, x^5)$ is about 6.0. Both PPWs are less than 6.0. If the short wave dominants the errors, it is expected that there is no big difference for these two schemes according to PPW analysis, which agrees with the Fig 3.14.

In Fig 3.15, the numerical results of the upwind CPR are compared with respect to bases $(1, x, x^2, x^3, x^4, x^5)$, and $\left(1, x, x^2, x^3, sin(4.0 * x), cos(4.0 * x)\right)$ for $\Delta x = 8.0$. Points-per-wavelength (PPW) is equal to 4.5 for the short wave. The optimized hybrid base's PPW is about 4.5 and the polynomial base's PPW is about 6.0. Therefore, it is expected that the optimized hybrid base should perform better than the corresponding polynomial base, because only the former base's PPW is close to the PPW requirement for the initial short wave and the latter's PPW 6.0 is much larger than the initial short wave PPW requirement 4.5. In Fig 3.15, the simulation results agree with our expectation. In other word, the hybrid base performs better than the corresponding polynomial bases.

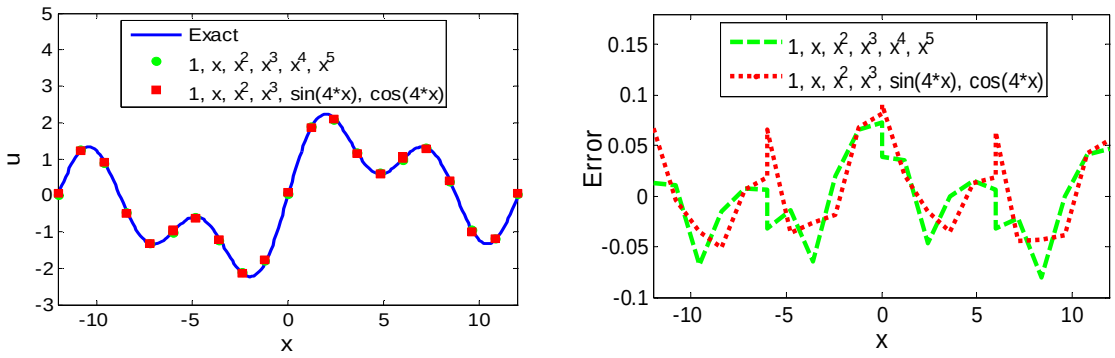

Figure 3.14. Comparison of a "broadband" wave at $\Delta x = 6.0$

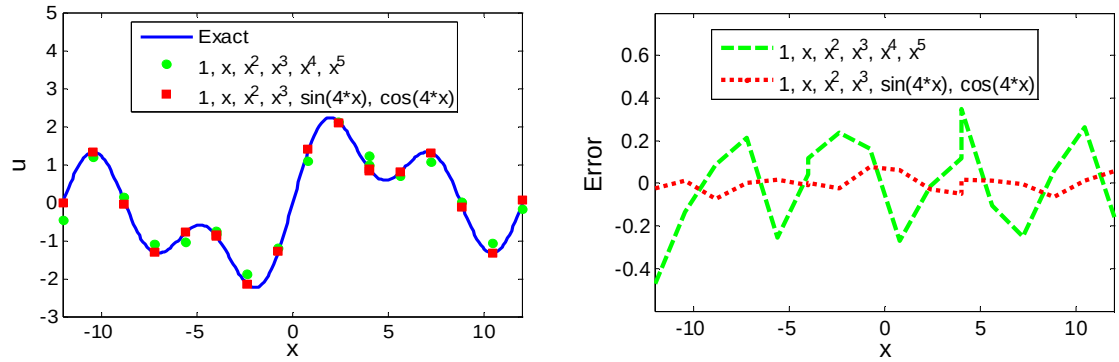

Figure 3.15. Comparison of a "broadband" wave at $\Delta x = 8.0$

CHAPTER 4. TWO-DIMENSIONAL WAVE PROPAGATION ANALYSIS

4.1 Wave Propagation Analysis

The extension of the wave propagation analysis to 2D is described in this section. We consider the 2D linear advection equation with periodic boundary condition mimicking the ideas by Hu [43] and Van den Abeele [87]

$$\frac{\partial u}{\partial t} + a_x \frac{\partial u}{\partial x} + a_y \frac{\partial u}{\partial y} = 0 \tag{4.1}$$

with $\vec{a} = \left[a_x \; a_y\right]^T = a\vec{I} = a[cos\psi \; sin\psi]^T$. The vector $\vec{a}$ is the wave propagation velocity and is defined by the Cartesian components a_x and a_y or defined by the amplitude a and the direction of the wave propagation ψ. A plane harmonic wave is given

$$u(t, \vec{r}) = \hat{u}(t) * \exp\left(I\vec{k} \cdot \vec{r} - I\omega t\right) \tag{4.2}$$

with $\vec{r} = [x \;\; y]^T$ and $k = k[cos\theta \;\; sin\theta]^T$, and θ is the orientation of the wave. Substituting the above equation into (4.1), the following exactly dispersion relation is obtained:

$$\omega = \|a\| k cos(\psi - \theta) \tag{4.3}$$

The numerical dispersion relation corresponding to a discretization of the linear advection Eq. (4.1) on a uniform quadrilateral cell grid, as shown Fig 4.1, with the upwind CPR formulation is compared with the exact dispersion relation to study the dispersion and dissipation behavior. As for the 1D analysis, all quantities in this section are non-dimensional. In the following sections, the upwind CPR formulation with hybrid bases for quadrilateral and triangle cell grids will be discussed.

The stability and accuracy of the upwind CPR formulation with hybrid bases are discussed in this section. The computational domain is divided into rectangular element E^{mn} by straight lines $x = x_n$ and $y = y_m$, i.e., $E^{nm} = [x_n, x_{n+1}] \times [y_m, y_{m+1}]$, as shown in Fig 4.1 Set $\delta_x = \delta_y, and\ \delta_x = x_{n+1} - x_n,\ \delta_y = x_{m+1} - x_m$.

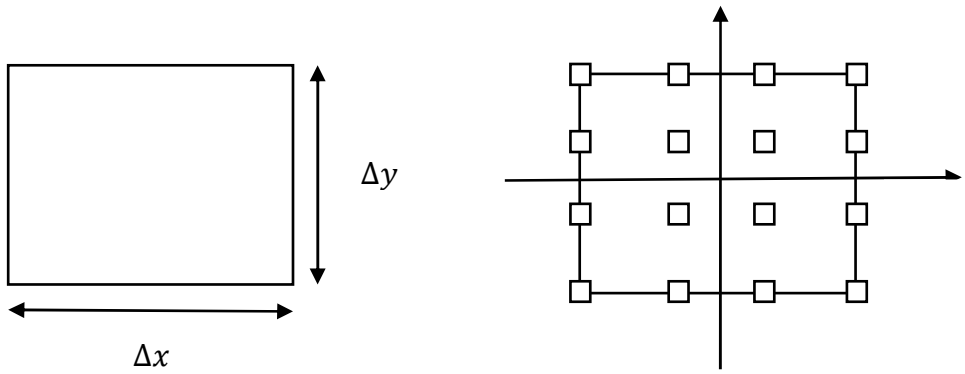

Figure 4.1. Rectangular mesh pattern and local coordinate system.

Then using upwind scheme and tensor product basis on $\in [-1,1] \times [-1,1]$, Eq. (4.1) can be written in the following form.

$$\frac{\partial \vec{\boldsymbol{u}}_{n,m}}{\partial t} + a_x * \left[N^0 \vec{\boldsymbol{u}}_{n,m} + N^{-1} \vec{\boldsymbol{u}}_{n-1,m}\right] + a_y * \left[M^0 \vec{\boldsymbol{u}}_{n,m} + M^{-1} \vec{\boldsymbol{u}}_{n,m-1}\right] = 0 \quad (4.4)$$

$\vec{\boldsymbol{u}}_{n,m}$ denotes the vector containing all the solution points in the local element $[-1,1] \times [-1,1]$. The matrix elements N^0, N^{-1}, M^0 and M^{-1} are given by in the Appendix D.

N^0, N^{-1}, M^0 and M^{-1} are defined in Appendix D. By supplying equation (4.2) and tensor product basis into Eq. (4.4), the numerical dispersion relation is given by

$$det\left(-I\tilde{\Omega} + cos\psi\left(e^{-iKcos\theta}N^{-1} + N^0\right) + sin\psi\left(e^{-iKsin\theta}M^{-1} + M^0\right)\right) = 0 \quad (4.5)$$

The determinant of the coefficient matrix must be zero for a non-trivial solution of u, that determines the dispersion relation for the semi-discretization equation. From Eq. (4.5) $\tilde{\Omega}$

should be found and compared to the non-dimensional exact frequency Ω, which is given by the exact dispersion relation $\Omega = Kcos(\theta - \psi)$. Equation (4.5) has $N * N$ eigenvalues and $N = k + 1$, corresponding to the eigenmodes of the numerical system. As same as the one dimensional analysis, the quantity $-I\tilde{\Omega}$ is also called Fourier footprint $\mathcal{R} = \mathcal{R}^{Re} + I\mathcal{R}^{Im}$ of the spatial discretization. The imaginary part $\mathcal{R}^{Im}$ is a measure of the dispersive properties of the scheme, whereas the real part $\mathcal{R}^{Re}$ reflects the diffusive behavior and should be non-positive for stable schemes for all of K, θ and ψ.

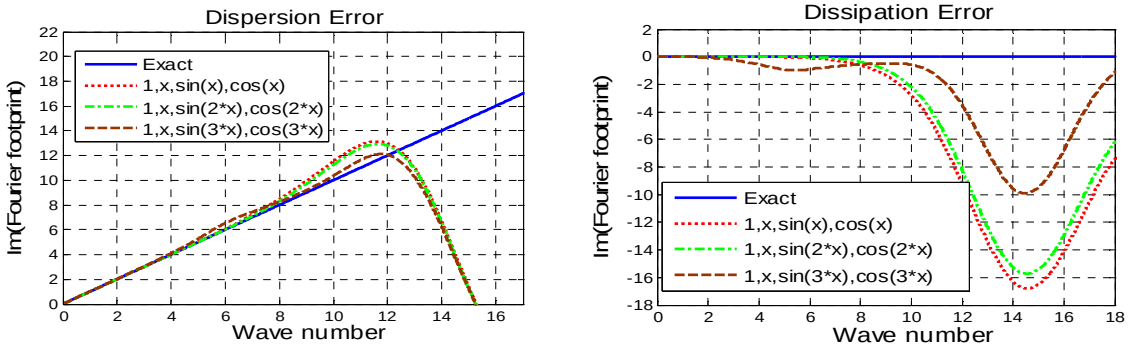

Figure 4.2. Dispersion and diffusion error as a function of the wave number for $\theta = \psi = \pi/6$

Fig 4.2 shows the eigenvalues of Eq. (4.5) as a function of the wave number K at $\theta = \psi = \pi/6$ for 4^{th} DOFs with hybrid tensor product bases. The choice of $\theta = \psi$ corresponds to a propagation direction parallel to the orientation of the plane wave. The exact dispersion relation is given by $\Omega = K$ in this case. For this choice, the wave length in the propagation direction is minimal, leading to the most severe test of the accuracy of the scheme. The wave propagation is anisotropic, especially for under-resolved waves. It can be concluded from the

right figure of Fig 4.2 that the scheme is stable for $\theta = \psi = \pi/6$, since $\mathcal{R}^{Re}$ are always non-positive.

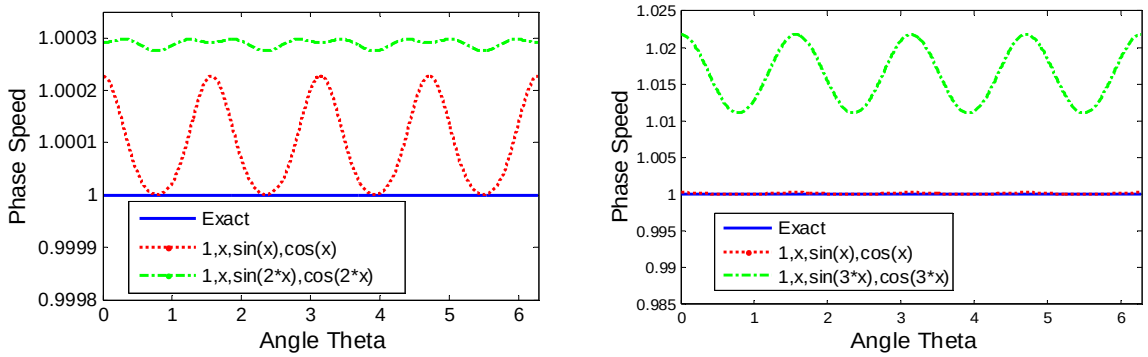

Figure 4.3. Phase speed $(\mathcal{R}^{Re}/K)$ as function of $\theta\ (=\psi)$ for $K = \pi$

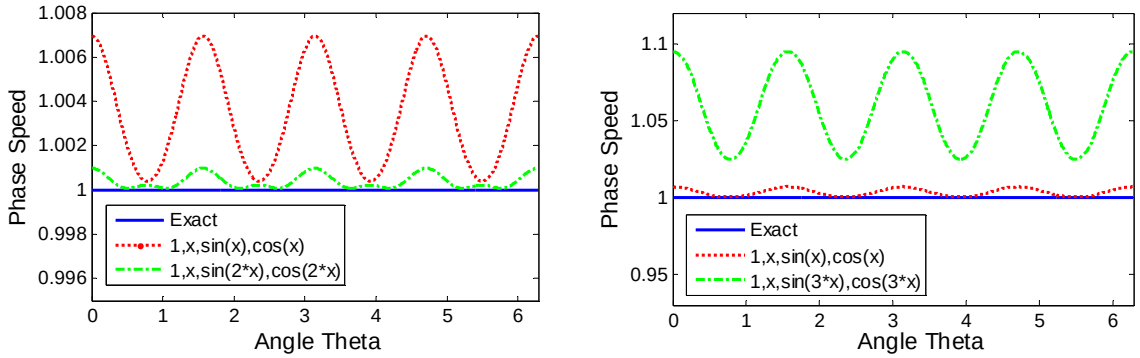

Figure 4.4. Phase speed $(\mathcal{R}^{Re}/K)$ as function of $\theta\ (=\psi)$ for $K = 1.5 * \pi$

In Fig 4.3, phase speed $(\mathcal{R}^{Re}/K)$ is plotted as a function of angle $(\theta = \psi)$ for $K = \pi$, and it is obvious that errors of $\big(1, x, sin(x), cos(x)\big)$ < errors of $\big(1, x, sin(2 * x), cos(2 * x)\big)$ < $\big(1, x, sin(3 * x), cos(3 * x)\big)$. In Fig 4.4, phase speed $(\mathcal{R}_{Re}/K)$ is plotted as a function of angle $(\theta = \psi)$ for $K = 1.5 * \pi$ and it is shown that that errors of $\big(1, x, sin(2 * x), cos(2 * x)\big)$ < errors of $\big(1, x, sin(x), cos(x)\big)$ < $\big(1, x, sin(3 * x), cos(3 * x)\big)$. It is obvious that the

errors of non-dimensional wave number $K = \pi$ are less than the errors of $K = 1.5 * \pi$ for dispersion errors.

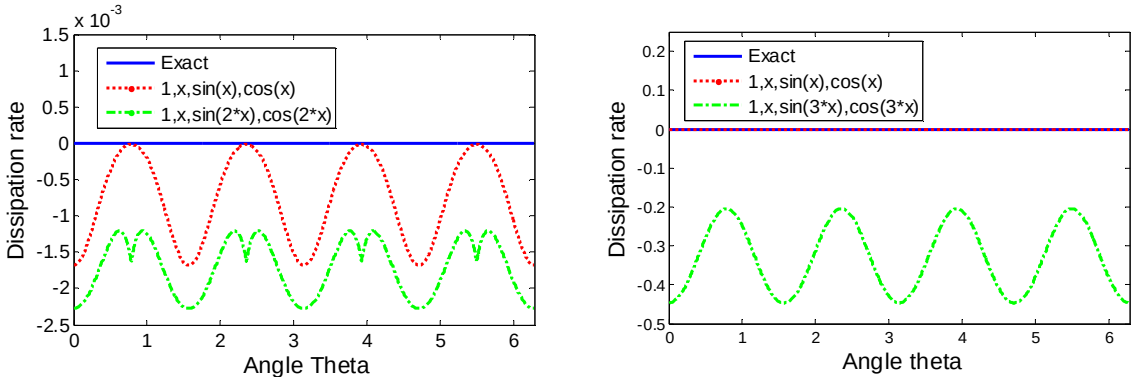

Figure 4.5. Dissipation rate ($\mathcal{R}^{Im}$) as function of θ $(= \psi)$ for $K = \pi$

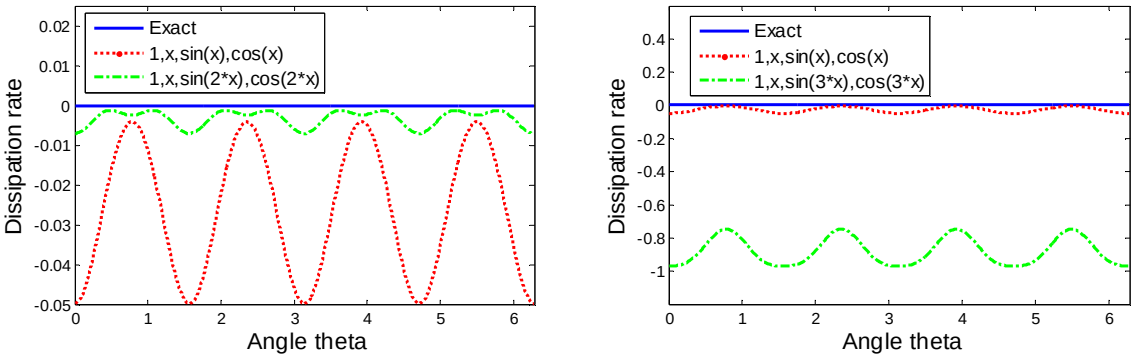

Figure 4.6. Dissipation rate ($\mathcal{R}^{Im}$) as function of θ $(= \psi)$ for $K = 1.5 * \pi$

In Fig 4.5, dissipation rate ($\mathcal{R}^{Im}$) is plotted as a function of angle $(\theta = \psi)$ for $K = \pi$, and it is obvious that errors of $(1, x, sin(x), cos(x))$ < errors of $(1, x, sin(2 * x), cos(2 * x))$ < $(1, x, sin(3 * x), cos(3 * x))$. In Fig 4.6, dissipation rate ($\mathcal{R}^{Im}$) is as a function of angle $(\theta = \psi)$ for $K = 1.5 * \pi$ and it is shown that that errors of $(1, x, sin(2 * x), cos(2 * x))$ < errors of $(1, x, sin(x), cos(x))$ < $(1, x, sin(3 * x), cos(3 * x))$. As same as the phase speed errors, that the errors of non-dimensional wave number $K = \pi$ are less than the errors of $K = 1.5 * \pi$ for dissipation errors.

It shows that the accuracy of different schemes depends on different non-dimensional wave numbers. It can be observed that the dissipation error is relatively larger than the dispersion error. All of above four Figures indicate that both the dispersion and dissipation errors are the largest in the direction of $\theta = 0$ or $\theta = \pi/2$, which can be verified by the dispersion relation (4.5). And the dispersion relation in the direction $\theta = 0$ or $\theta = \pi/2$ is the same as the corresponding previous one-dimensional analysis.

4.2 Numerical Test

4.2.1 Two-Dimensional Acoustic Wave Propagation

The propagation of acoustic waves generated by an acoustic pulse is simulated in 2D. The acoustic perturbations have small amplitude compared to the ambient flow variables. The exact solution to the LEEs for these problems can thus be used as a reference. The governing equations for the 2D non-linear Euler equations

$$\frac{\partial Q}{\partial t} + \frac{\partial E}{\partial x} + \frac{\partial F}{\partial y} = 0 \tag{4.6}$$

where Q, E and F are vectors given by

$$Q = \begin{Bmatrix} \rho \\ \rho u \\ \rho v \\ \rho E \end{Bmatrix}, \quad E = \begin{Bmatrix} \rho u \\ \rho u^2 + p \\ \rho uv \\ u(\rho E + p) \end{Bmatrix}, \quad F = \begin{Bmatrix} \rho v \\ \rho uv \\ \rho v^2 + p \\ v(\rho E + p) \end{Bmatrix} \tag{4.7}$$

with ρ the mass density, u and v the velocity components in x and y directions and p the pressure. The total energy E is defined by the following equation

$$E = \frac{1}{\gamma - 1}\frac{p}{\rho} + \frac{u^2 + v^2}{2} \tag{4.8}$$

where γ is set to 1.4 which is the ratio of specific heat to air. The initial solution is an acoustic pulse with a Gaussian profile and is set as same as one by Kris [67, 69]

$$\rho = \rho_\infty \left(1 + 0.001 * exp\left(-\frac{(x-0.5)^2 + (y-0.5)^2}{\gamma_0^2}\right)\right) \tag{4.9}$$

$$P = P_\infty + c_\infty^2(\rho - \rho_\infty) \tag{4.10}$$

$$u = 0 \tag{4.11}$$

$$v = 0 \tag{4.12}$$

And the ambient pressure, mass density and the half-width of the Gaussian profile are given as follow

$$P_\infty = 1, \quad \rho_\infty = 1, \quad r_0 = 0.05 \tag{4.13}$$

The exact solution of the LEEs for the acoustic pressure field is given as

$$P_{ac}(t,x,y) = P - P_\infty = 0.001 * \frac{c_\infty^2 b^2}{2} \int_0^{+\infty} exp\left(-\left(\frac{\xi b}{2}\right)^2\right) cos(\xi c_\infty t) J_0(\xi t) \xi d\xi \tag{4.14}$$

with $\eta = \sqrt{(x-0.5)^2 + (y-0.5)^2}$ and J_0 is the zero-th order Bessel function of the first kind which is used as a reference solution referring to [44] and [46]. b is the halfwidth of the Gaussian profile and is set as 0.05.

The domain under considerations is a square with an edge length equal to one, $[0,1] \times [0,1]$. This domain is discretized by a uniform Cartesian grid. The computations are carried out on three different structure grids (5×5), (10×10) and (20×20) on a square domain $[0,1] \times [0,1]$. Roe's scheme is used as approximate Riemann solver. Time marching was done with a fourth-order, four stage R-K scheme. And all numerical tests are carried out with $\Delta t = 0.0001s$, $T = 0.3S$ and Gauss-Lobatto points are used as distribution points for each element for CPR schemes. Structured quadrilateral 10×10 grids are given on left of Fig 4.7

and pressure contours are given on the right of Fig 4.7 which is based on tensor product basis with approximation spaces $(1, x, x^2, x^3)$. Wave has not yet reached the boundary of the computational domain at $T = 0.3S$ and thus the far field boundary condition has no influence on the solution.

The profiles of the acoustic pressure $y = 0.5$ at $T = 0.3S$ along with the exact acoustic pressure solution of the LEEs are plotted based on the upwind CPR schemes based on hybrid bases with different parameters. We focus on the comparison of the results between the optimized hybrid bases and other hybrid bases.

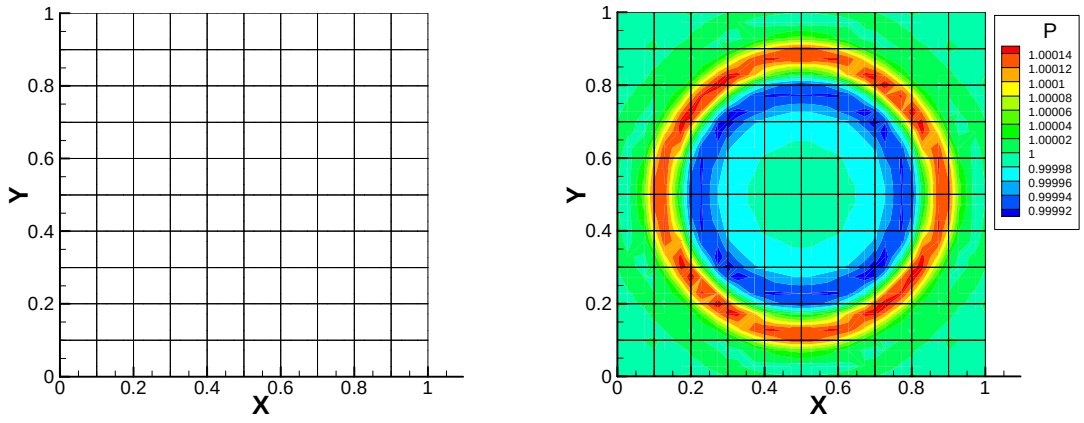

Figure 4.7. Structured quadrilateral 10×10 grids (left) and pressure contours (right) based on tensor product basis with polynomial approximation spaces

The numerical results of 4th DOFs are compared in Fig 4.8 and Fig 4.9. In fig 4.8, errors of the optimized bases $\left(1, x, \sin(2 * x), cos(2 * x)\right)$ are smallest among all of approximate bases shown on the fig based on 10×10 grids. This property agrees with the previous analysis that the optimized hybrid bases shows better dispersion and dissipation properties when non-dimensional wave numbers of the schemes are given in a certain range. In Fig 4.9 the optimized base still performs better than the corresponding polynomial base based on

20×20 grids. The difference between the optimized hybrid base and the other hybrid bases becomes smaller. It can be expected that the polynomial base will perform best when the grids are fine enough.

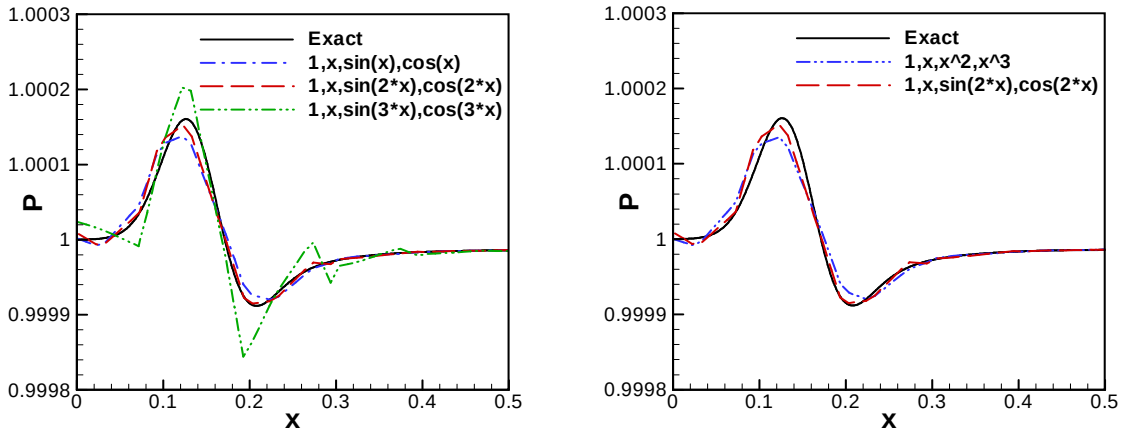

Figure 4.8. Pressure distribution at $y = 0.5$ on 10×10 grids with $\Delta t = 0.0001s,\ T = 0.3S$ for 4 DOFs

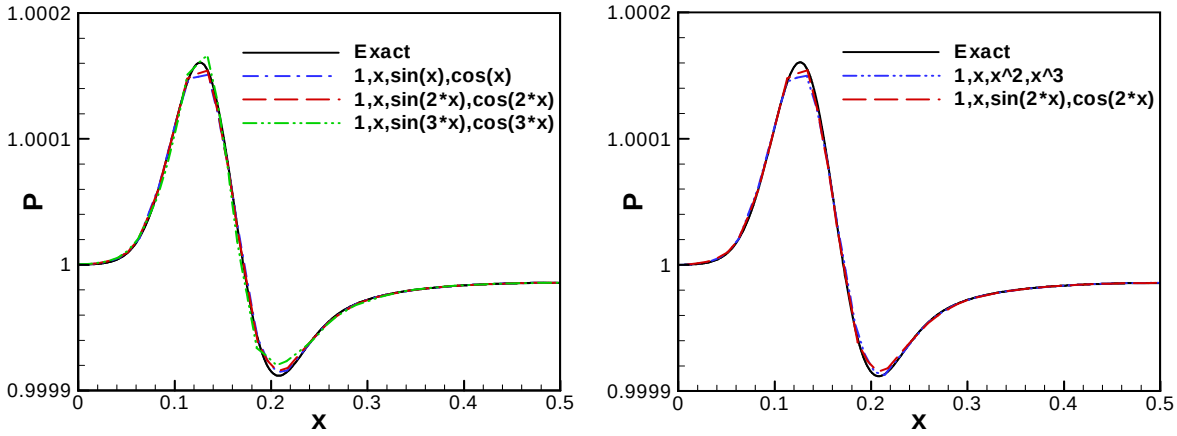

Figure 4.9. Pressure distribution at $y = 0.5$ on 20×20 grids with $\Delta t = 0.0001s,\ T = 0.3S$ for 4 DOFs

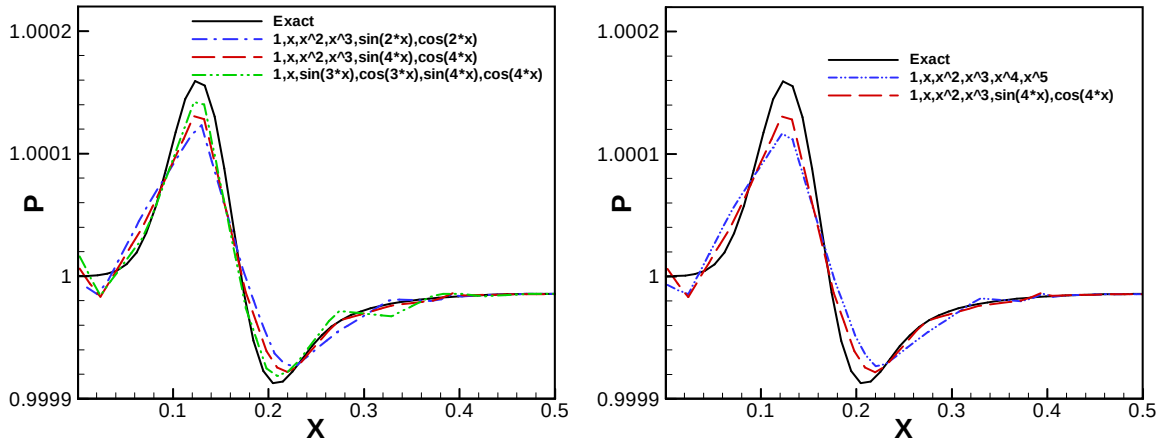

Figure 4.10. Pressure distribution at $y = 0.5$ on 5×5 grids with $\Delta t = 0.0001s,\ T = 0.3S$ for 6 DOFs

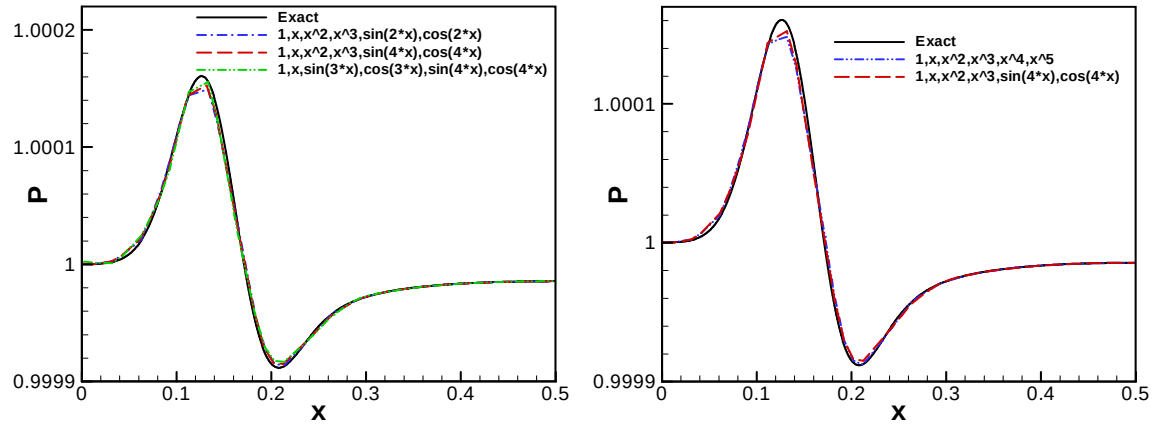

Figure 4.11. Pressure distribution at $y = 0.5$ on 10×10 grids with $\Delta t = 0.0001s,\ T = 0.3S$ for 6 DOFs

The numerical results of 6th DOFs are compared in Fig 4.10 and Fig 4.11 on 5×5 and 10×10 grids. In both Fig 4.10 and Fig 4.11, the optimized base $(1, x, sin(3.0 * x), cos(3.0 * x), sin(4.5 * x), cos(4.5 * x))$ performed better than the optimized base $(1, x,\ x^2,\ x^3,\ sin(4.0 * x), cos(4.0 * x))$, and the latter performed better than the

corresponding polynomial bases. It is clear that when the grids become fine enough, the polynomial bases will perform best. These results agree with our previous Fourier analysis, that the optimized hybrid bases show advantages in a certain non-dimensional wave number range. It is obvious that the more Fourier components there are, the more accurate results there are.

CHAPTER 5. GRID RESOLUTION STUDY FOR VISCOUS FLOW

In this chapter, extensive grid resolution studies are performed for both 1D and 2D viscous burger's equations with exact solutions, with the objective of understanding the mesh size requirement to resolve a viscous boundary layer using high-order methods. It is well known that the mesh size, which is defined from non-dimensional wall distance $y^+ = 1$, gives accepted results to simulate viscous boundary layer problem for 2nd order finite volume method. For high-order CPR formulation, what grid size y^+ is required to match the results from the 2nd order finite volume method with $y^+ = 1$.

1D and 2D burger's equation are used as the viscous boundary layer model problem. Skin friction is used as the indicator of accuracy for the resolution of a boundary layer. LDG is employed to discretize the diffusion term to achieve the $(k+1)th$ order of accuracy with a degree k polynomial approximation.

5.1 1D Convection and Diffusion Equation

5.1.1 Introduction to 1D Convection and Diffusion Equation

1D viscous burger's equation, which is solved as a boundary layer problem, is given as follows

$$u_t + u \cdot u_y - \mu u_{yy} = 0, \qquad y \in (0,1) \tag{5.1}$$

with the following initial and boundary conditions:

$$u(y,0) = -tanh\left(\frac{y}{2\mu}\right) \tag{5.2}$$

$$u(0,t) = 0, \qquad u(1,t) = -tanh\left(\frac{1}{2\mu}\right) \tag{5.3}$$

The problem has the following exact solution:

$$u(y,0) = -tanh\left(\frac{y}{2\mu}\right) \tag{5.4}$$

where $\mu = 0.01$.

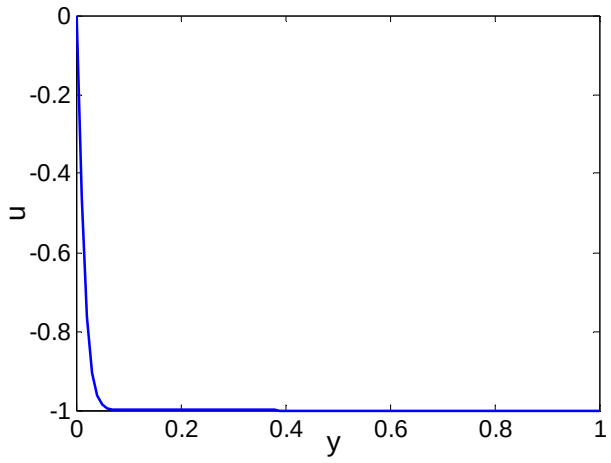

Figure 5.1 Exact solution of u given in (5.4)

As we known, the viscous boundary layer regions remain closed to the body surface. The exact solution (5.4) in Fig 5.1 shows a boundary layer characteristic, because the velocity changes to a constant value in a small regions closed to the initial y-coordinates. We use this 1D viscous burgers equation to study the grid resolution for various orders of CPR formulation. In the boundary layer, the skin friction coefficient C_f is defined as

$$C_f = \frac{\tau_w}{\frac{1}{2}\rho U_\infty^2} \tag{5.5}$$

where τ_w is the local shear stress, $\rho = 1$ is the fluid density and U_∞ is the free-stream velocity (usually taken outside of the boundary layer or at the inlet). The wall shear stress τ_w is given by

$$\tau_w = \mu \left(\frac{\partial u}{\partial y}\right)_{y=0} \tag{5.6}$$

where μ is the dynamic viscosity, and u is the flow velocity parallel to the wall. In this case, the wall is referred to $y = 0$, the u is the flow velocity. And $U_\infty = -1$ is the velocity outside of the boundary layer. Non-dimensional wall distance for a wall-bounded flow is defined in the following way

$$y^+ = \frac{\Delta y * u_\tau}{\nu} \tag{5.7}$$

where u_τ is the friction velocity at the nearest wall, Δy is the distance to the nearest wall and ν is the local kinematic viscosity of the fluid. y^+ is often referred to simply as y plus and commonly used in boundary layer theory and defining the law of the wall.

The friction velocity u_τ is defined as

$$u_\tau = \sqrt{\tau_w/\rho} \tag{5.8}$$

In order to get the skin friction coefficients based on the non-dimensional wall distance, steps are given here to follow.

- Step 1, set non-dimensional wall distance $y^+ = 1$ to derive Δy, which is the distance to the wall.

$$y^+ = \frac{\Delta y * u_\tau}{\nu} = 1 \Rightarrow \Delta y = \frac{y^+ * \nu}{u_\tau} = \frac{\nu}{u_\tau} \tag{5.9}$$

Substitute (5.8) into (5.9) to get the following equation

$$\Delta y = \frac{\nu}{u_\tau} = \frac{\nu}{\sqrt{\tau_w/\rho}} \tag{5.10}$$

Apply (5.6) into (5.10) to get

$$\Delta y = \frac{\nu}{\sqrt{\tau_w/\rho}} = \frac{\nu}{\sqrt{\mu\left(\frac{\partial u}{\partial x}\right)_{x=0}/\rho}} \tag{5.11}$$

- Step 2, set Δy as the grid size, which is derived from the exact solution, as a grid size to calculate the shear stress for different order of CPR schemes and 2nd order finite volume scheme.
- Step 3, different grid size Δy are found for different order CPR formulation to achieve a certain skin friction.

5.1.2 Different Viscous discretization Methods

Treatment of viscous terms has been discussed in chapter 2. In this section, two different viscous formulations are tested. The first formulation is the BR1 [9], the other formulation is the LDG [28].

5.1.2.1 Bassi-Rebay 1 (BR1)

Bassi and Rebay [9] proposed a method to discretize the diffusion term, which is named as BR1. Both unknown and its gradient are approximated in the polynomial approximation functions. Both the common numerical flux and auxiliary variable R are taken as the average between the two interface states.

$$u_i^{com} = \frac{u_{i-} + u_{i+}}{2} \quad \text{and} \quad R_i^{com} = \frac{R_{i-} + R_{i+}}{2} \tag{5.12}$$

The accuracy of the 4th order CPR formulation is tested in this case. Gauss-Lobatto point distribution is applied. The polynomial approximations space is used as the approximation reconstruction. The L_∞ and L_1 errors are presented in Table 5.1.

Table 5.1. The L_∞ and L_1 errors and orders of accuracy with BR1 method

Degree of Freedom	dx	L_∞ Error	L_∞ order	L_1 errors	L_1 order
4	0.04	4.7334e-02		7.9359e-04	
	0.02	7.3279e-03	2.69	9.1589e-05	3.12
	0.01	6.7790e-04	3.43	7.6026e-06	3.59
	0.005	7.5080e-05	3.17	7.9769e-07	3.25
	0.0025	8.4658e-06	3.15	7.4540e-08	3.42

These results did not match the expected the order of accuracy. It has been verified numerically in [79, 113], that this formulation leads to numerically stable but incorrect solutions. From the table 5.1, we can see that the numerical solutions seem to converge with mesh refinements but lost more half order of accuracy, especially for L_∞ errors. If one does a mesh refinement study without knowing the exact solution, one could conclude the method is convergent. If the method is used to solve the complicated Navier-Stokes equation, one could not be able to tell the result is wrong. This kind of results is very dangerous.

5.1.2.2 LDG Formulation

For the diffusion terms, the central fluxes (average values between the two interface states) is applied in the last section, but it turns out inconsistent solutions. In order to remedy the first formulation, the LDG method is applied as the second formulation to discretize the diffusion terms.

- The numerical flux function u is defined as the left values of the interface states and the right value between the two interface states, i.e., as

$$u_i^{com} = u_{i-} \qquad \text{and} \qquad R_i^{com} = R_{i+} \tag{5.13}$$

We also can alternately take the left and right limits for the flux in u and R. In other words, u_{i+} and R_{i-} are taken as the fluxes.

In Table 5.2, for illustration purpose that the L_∞ and L_1 errors are numerically observed orders of accuracy until convergence. Note that the LDG approach is capable of achieving the optimum $(k+1)$th order of accuracy in this case. For the following analysis, the LDG method is applied.

Table 5.2. The L_∞ and L_1 errors and orders of accuracy with LDG method

Degree of Freedom	dx	L_∞ Error	L_∞ order	L_1 errors	L_1 order
4	0.04	2.3207e-02		3.4881e-04	
	0.02	4.0084e-03	2.53	3.4244e-05	3.35
	0.01	2.3361e-04	4.10	1.8618e-06	4.20
	0.005	1.8334e-05	3.67	1.1231e-07	4.05
	0.0025	1.1745e-06	3.96	7.0211e-08	4.00

5.1.3 Grid Resolution Study

The 2nd order finite volume method is applied to compare with various orders of CPR schemes. Both node center and cell center finite volume schemes are considered. The face flux term is replaced with a common Riemann flux

$$F_{i+1/2} = \frac{F_i + F_{i+1}}{2} - \frac{1}{2}\left|\bar{u}_{i+1/2}\right|(u_{i+1} - u_i) \tag{5.16}$$

where $\bar{u}_{i+1/2} = (u_i + u_{i+1})/2$ and $F = u^2/2$. Monotone upstream-centered schemes for conservations laws (MUSCL) approach is applied for the variable extrapolation approach. The second-order upwind MUSCL approach is given as follows

$$u^l_{i+1/2} = u_i + \frac{1}{2} * (u_{i+1} - u_i); \quad u^r_{i+\frac{1}{2}} = u_{i+1} - \frac{1}{2} * (u_{i+2} - u_{i+1});$$
$$u^l_{i-1/2} = u_{i-1} + \frac{1}{2} * (u_i - u_{i-1}); \quad u^r_{i-\frac{1}{2}} = u_i - \frac{1}{2} * (u_{i+1} - u_i); \tag{5.17}$$

Table 5.3. The L_∞ and L_1 errors for 2nd order node center finite volume method

dx	L_∞ Error	L_∞ order	L_1 errors	L_1 order
0.01	2.8426e-02		1.0660e-03	
0.005	9.16 04e-03	1.63	3.1111e-04	1.78
0.0025	2.4849e-03	1.88	8.3827e-05	1.89
0.00125	6.4535e-04	1.95	2.1674e-05	1.95

Table 5.4. The L_∞ and L_1 errors for 2nd order cell center finite volume method

dx	L_∞ Error	L_∞ order	L_1 errors	L_1 order
0.01	2.8565e-02		1.0205e-03	
0.005	9.0022e-03	1.67	3.0877e-04	1.72
0.0025	2.4928e-03	1.85	8.3674e-05	1.88
0.00125	6.4517e-04	1.95	2.1654e-05	1.95

where l and r represent left and right values between the control volume interfaces.

In Table 5.3 and 5.4, the L_∞ and L_1 errors for 2nd order node center and cell center finite volume method are presented. Both FV methods achieve the expected order of accuracy.

5.1.3.1 Skin Friction Comparison based on Certain Grid Sizes

As we mentioned previously, the skin friction is used as the indicator of accuracy for the resolution of a boundary layer. The procedures how to get the skin friction are given as follows, which have been mentioned in section 5.1.1.

The dimensionless wall distance $y^+ = 1$, $y^+ = \frac{\Delta y * u_\tau}{\nu} = 1 \Rightarrow \Delta y = \frac{\nu}{u_\tau}$ and $u_\tau = \sqrt{\tau_w/\rho} \Rightarrow \Delta y = \frac{\nu}{\sqrt{\tau_w/\rho}}$ and set $\mu = 0.01, \rho = 1.0$. Analytical result is obtained from the exact solution $u(x,t) = -tanh\left(\frac{x}{2\mu}\right)$. The wall shear stress is given as follows

$$|\tau_w| = \mu \left|\frac{\partial u}{\partial x}\right|_{x=0} = |0.01 * (-50)| = 0.5 \tag{5.18}$$

So the skin friction is given as

$$C_f = \frac{\tau_w}{\frac{1}{2}\rho U_\infty^2} = 1.0 \tag{5.19}$$

The friction velocity u_τ is given as

$$\xrightarrow{yields} u_\tau = \sqrt{\tau_w/\rho} = \sqrt{0.5} = 0.7071 \tag{5.20}$$

Δy corresponding to $y^+ = 1$ is given as

$$\Delta y = \frac{y^+ * \nu}{u_\tau} = \frac{1.0 * 0.01}{0.7071} = 0.01414 \tag{5.21}$$

There are $(k+1)$ degrees of freedom within one element for $(k+1)th$ order CPR formulation. To make a fair comparison between skin frictions of the finite volume schemes and those of the CPR formulation, the Δy should be scaled with a factor $(k+1)$, to take into account the higher number of degrees of freedom used by the CPR formulation.

Table 5.5 Skin frictions comparison

with $\Delta y = 0.01414$ ($y^+ = 1$)

	FV 1	FV 2	2nd order CPR	3rd order CPR	4th order CPR	5th order CPR	6th order CPR
Δy	0.01414	0.01414	0.01414*2	0.01414*3	0.01414*4	0.01414*5	0.01414*6
SF	0.9034	0.9784	0.9712	0.9996	1.0000	1.0000	1.0000

In table 5.5, $\Delta y = 0.01414$ is set as the grid size to calculate skin frictions. SF represents skin friction, and FV1 and FV2 represent 2nd order node and cell center finite volume methods, respectively. It is obvious that the higher order CPR schemes achieve better results.

5.1.3.2 y^+ Comparison based on Certain Skin Friction

In Table 5.6 and 5.7, Δy are compared for different order CPR schemes with a certain skin friction. In Table 5.6, the skin friction is equal to 0.9034 for 2nd order node center FV method, when $y^+ = 1$. For the same skin friction, y^+ is equal to 39.6322 for 6th order CPR schemes. In Table 5.7, the skin friction is equal to 0.9784 for 2nd order cell center FV method, when $y^+ = 1$. For this skin friction, y^+ is equal to 23.6351 for 6th order CPR schemes. This means that when a certain skin friction is required, a larger grid size is needed for high order CPR schemes. All of calculation is based on polynomial reconstruction and uniform point distribution within each element for CPR method.

For this 1D convection-diffusion problem the boundary layer is $\delta = 0.054$ when $u = 0.99$ from the exact solution (5.4). The boundary layer $\delta = 0.054$ is set as the grid size to compute the skin friction for both 2nd finite volume method and various order CPR

formulation. In Table 5.8, the skin frictions are presented. It is obvious that the higher order the CPR formulation is and the larger skin friction is.

Table 5.6 y^+ comparison with a fixed skin friction SF = 0.9034

	FV 1	FV 2	2nd order CPR	3rd order CPR	4th order CPR	5th order CPR	6th order CPR
Δy	0.01414	0.02960	0.02916*2	0.04706*3	0.0646*4	0.08228*5	0.0934*6
y^+	1.0000	2.0934	4.1244	9.9844	18.2744	29.0948	39.6322

Table 5.7 y^+ comparison with a fixed skin friction SF = 0.9784

	FV 1	FV 2	2nd order CPR	3rd order CPR	4th order CPR	5th order CPR	6th order CPR
Δy	0.00528	0.01414	0.01300*2	0.02386*3	0.03460*4	0.04515*5	0.05570*6
y^+	0.3734	1.0000	1.8388	5.0622	9.7880	15.9653	23.6351

Table 5.8 Skin friction comparison

with the boundary layer $\delta = 0.054$ when $u = 0.99$

	FV 1	FV 2	2nd order CPR	3rd order CPR	4th order CPR	5th order CPR	6th order CPR
Δy	0.054	0.054	0.054*2	0.054*3	0.054*4	0.054*5	0.054*6
SF	0.1623	0.2828	0.2830	0.3766	0.4361	0.4694	0.4860

5.1.3.3 Solution Points Distribution Study

The point distribution influence within an element is studied in this section. In Table 5.9, the uniform and Gauss-Lobatto point distribution are presented with comparison to the 2nd order FV methods. The uniform point and Gauss-Lobatto point distribution values in the

standard local coordinates are $\xi: [-1, -1/3, 1/3, 1]$ and $\xi: [-1, -\sqrt{5}/5, \sqrt{5}/5, 1]$, respectively. In Table 5.9, Gauss-Lobatto point distribution shows a better result than the uniform point distribution.

Table 5.9. y^+ comparison with the fixed skin friction SF = 0.9784 for different point distribution 4th order CPR

	FV 1	FV 2	Lobatto points	uniform points
Δy	0.00528	0.01414	0.03460*4	0.03380*4
y^+	0.3734	1.0000	9.7880	9.5615

Table 5.10. y^+ comparison with the fixed skin friction SF = 0.9784 for 4th order CPR with different point distribution

	FV 2	d1	d2	d3	d4	d5
Δy	0.01414	0.03380*4	0.03415*4	0.03460*4	0.03480*4	0.03505*4
y^+	1.00	9.56	9.68	9.79	9.84	9.92

Table 5.11. y^+ comparison with the fixed skin friction SF = 0.9784 for 4th order CPR with different point distribution

	FV 2	d6	d7	d8	d9	d10
Δy	0.01414	0.03505*4	0.03630*4	0.03820*4	0.03960*4	0.04138*4
y^+	1.00	9.92	10.28	10.80	11.20	11.71

Table 5.10 and 5.11 show y^+ comparison based on different point distribution $\xi: [-1, -d, d, 1]$. d is changed from small to large, in other words, from uniform values to

the values closed to element interface. In table 5.10, d1 = 0.3333, d2 = 0.3903, d3 = 0.4472, d4 = 0.4736 and d5 = 0.5000. In table 5.11, d6 = 0.5000, d7 = 0.6000, d8 = 0.7000, d9 = 0.7500, and d10 = 0.8000. It is obvious that when the d approaches to the boundary of the element, the required y^+ beomes larger.

Convergent histories are presented in Fig 5.2 for different point distribution based on grid size $\Delta y = 0.01414 * 4$, which corresponds to $y^+ = 1$ for each degree of freedom for 4^{th} order CPR formulation. When the point distribution is approaching to the element interface, the convergence is slow as a compromise for the more accurate results.

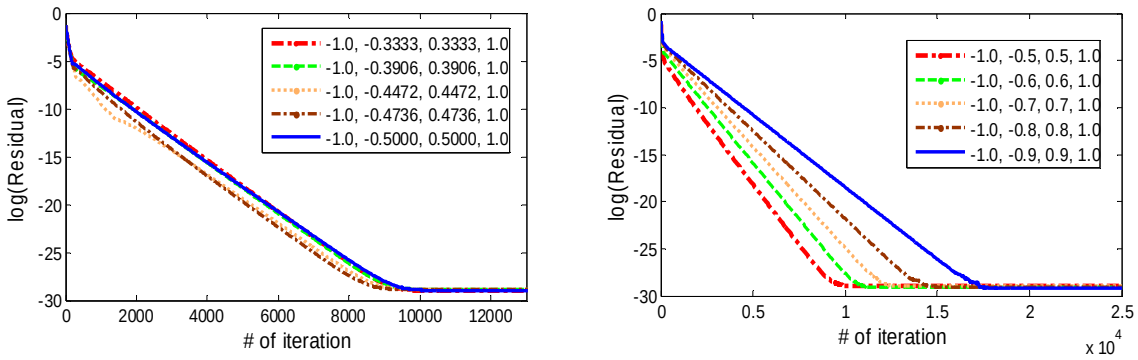

Figure 5.2. Comparison of convergence history for different point distributions with $y^+ = 1$ for each DOF

5.2 2D Convection and Diffusion Equation

5.2.1 Introduction to 2D Convection and Diffusion Equation

In this section, extensive accuracy studies were carried out for 2D convection and diffusion equation. Following a similar procedure for 1D viscous burgers equation, 2D

viscous burgers equation are designed to test the resolution for different order CPR formulation with exact solutions.

We use the similar manufactured solution of Sun [78]. The convection-diffusion equation has its inviscid and viscid fluxes defined as $F_i = \vec{\beta}u$ and $F_v = \overline{\mu} \cdot \nabla u$, respectively, where $\vec{\beta}$ is the advection and $\overline{\mu}$ is isotropic, its notation is replaced by a scalar μ. The convection velocity is set as uniform and horizontal with a unit magnitude for the linear viscous burgers equation and a diffusivity of $\mu = 10^{-8}$ is employed. The computational domain is rectangular box of $[0.05,1.05] \times [0,0.001]$ to avoid the leading edge singularity problem. This 2D convection-diffusion equation is defined as

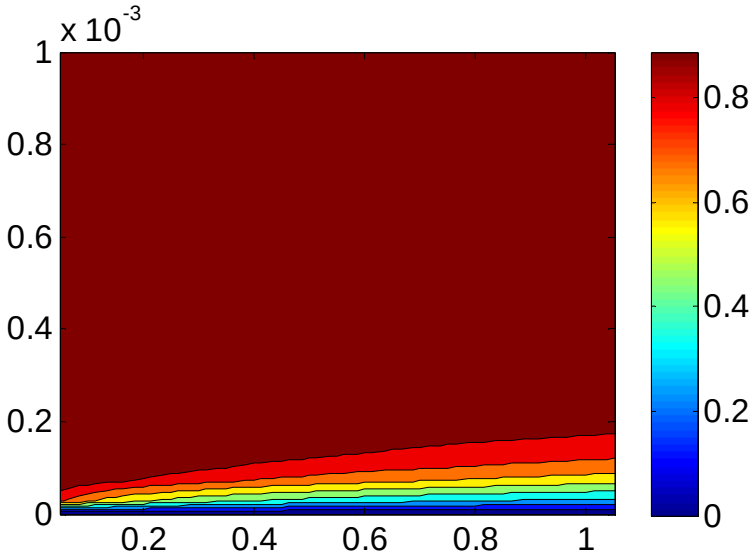

Figure 5.3 Exact solution of u given in (5.23)

$$u_t + u_x - \mu(u_{xx} + u_{yy}) = 0 \tag{5.22}$$

A source term is added such that the exact solution to this problem has a form of

$$U = 1 - e^{\frac{-y}{\sqrt{c\mu x}}} \tag{5.23}$$

with $c = 0.59$. This solution is shown in Fig 5.3 and represents a thin boundary layer growing with $\sqrt{x}$ along the bottom wall. It has a thickness of $\delta_{0.99} = 8 * 10^{-5}$ at the inflow and $3.6 * 10^{-4}$ at the outflow. Note that the leading edge of the boundary layer is not included in the computation domain.

5.2.2 Method of Manufacture Solutions (MMS)

In order to assess the accuracy of the discretization methods of the previous section, exact solutions are required. To address this problem, Roache [75] proposed the Method of Manufactured Solutions, which provides a general procedure for generating an analytical solution for code accuracy verification. The method is straightforward and leaded to complete and final code verification. The basic idea of the procedure is to manufacture an exact solution without being concerned about its physical realism. A continuum solution independent of the code or of the hosted equations is picked up and be used to verify codes. A non-trivial analytical solution which exercises all ordered derivatives is used. In MMS, instead of solving equation (5.22) directly, we solve the equation augmented with an analytical source term,

$$u_t + u_x - \mu(u_{xx} + u_{yy}) = H(x, y) \tag{5.24}$$

Once an arbitrary manufactured solution is selected, the source term is found by substituting the exact solution into the original continuous differential equation and setting the source term to the remainder. The source term is not a function of u, but is only a function of the independent variables and parameters of the PDE. The chosen exact solution (5.23) is used.

We determine the source term $H(x,y)$ which, when added the Burgers equation for $u(x,y)$, produces the exact solution. We write the Burgers equation as an operator (linear) of u,

$$L(u) = u_t + u_x - \mu\left(u_{xx} + u_{yy}\right) \tag{5.25}$$

We evaluate the u that produce the exact solution by operating on the exact solution with $L(u)$. Substitute the exact solution into equation (5.37) to get the source term $H(x,y)$.

$$H(x,y) = \ L(U) = U_t + U_x - \mu\left(U_{xx} + U_{yy}\right) \tag{5.26}$$

Matlab symbolic calculation is applied here to get $H(x,y)$ as following

$$H(x,y) = 4x^2 \ + \ y^2 \ - \frac{2c^3\mu^2x^4y}{(c\mu x)^{\frac{5}{2}}} - \frac{3c^3\mu^3x^3y}{(c\mu x)^{\frac{5}{2}} * \left(4cx^3e^{\frac{y}{(c\mu x)^{\frac{1}{2}}}}\right)} \tag{5.27}$$

Then we now solve the modified equation

$$L(u) \equiv u_t + u_x - \mu\left(u_{xx} + u_{yy}\right) = H(x,y) \tag{5.28}$$

Or

$$u_t = -u_x + \mu\left(u_{xx} + u_{yy}\right) + H(x,y) \tag{5.29}$$

with compatible initial and boundary conditions, the exact solution will be $U(x,y)$ given by (5.35).

5.2.3 Grid Resolution Study

The computational domain is divided into rectangular elements E^{nm} by lines $x = x_n$ and $y = y_m$, i.e., $E^{nm} = [x_n, x_{n+1}] \times [y_m, y_{m+1}]$. The basis in this section is formed by a tensor product of one-dimensional polynomial basis. In table 5.12, the L_∞ and L_1 errors are

presented. Note that the approach is capable of achieving the optimum 4th order of accuracy with degree 3 polynomial reconstruction.

Table 5.12 The L_∞ and L_1 errors and order of accuracy for 4th order CPR

Grid size	L_∞ Error	Order	L_1 Error	Order
20x10	2.354e-01		1.134e-03	
40x20	4.239e-02	2.47	1.207e-04	3.23
80x40	5.478e-03	2.95	1.018e-05	3.56
160x80	4.826e-04	3.50	7.455e-07	3.77
320x160	3.188e-05	3.92	4.692e-08	3.99

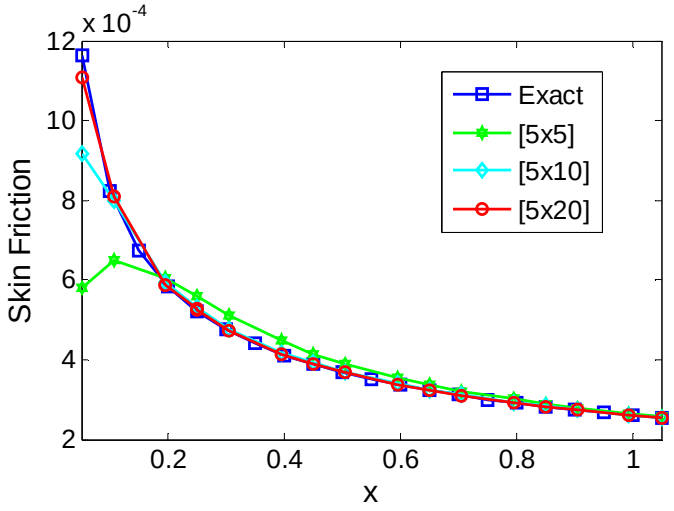

Figure 5.4. Skin frictions comparison with different grids in y-direction for 4th order CPR

In Fig 5.4, numerical skin frictions are presented for three different grids $[5 \times 5], [5 \times 10]$, and $[5 \times 20]$ compared with the skin frictions from the exact solution with 4th order

CPR formulation. We kept the same grids in the x-direction, and use different grids in the y-direction. It is obvious that the finer grids gave better numerical results.

In Fig 5.5, numerical skin frictions are presented for three different grids $[5 \times 5], [10 \times 5]$, and $[20 \times 5]$ compared with the skin frictions from the exact solution with 4th order CPR formulation. We kept the same grids in the y-direction, and use different grids in the x-direction. It is obvious that there is no big difference for different grid size.

In Fig 5.6, numerical skin frictions are presented for 2nd, 4th and 6th order CPR formulation for grids $[5 \times 5]$ compared with the skin frictions from the exact solution. Of course the higher order formulations give better numerical results.

The numerical skin frictions of various order CPR formulation are studied for more details. If we set $x = 1.05$, the exact solution is

$$u = 1 - e^{-\frac{y}{\sqrt{C\mu * 1.05}}} \tag{5.43}$$

The wall shear stress is given as follows

$$|\tau_w| = \mu \left|\frac{\partial u}{\partial x}\right|_{x=0} = |1.0e-08 * 1.7554e+04| = 1.2705e-04 \tag{5.44}$$

So the skin friction is given as

$$C_f = \frac{\tau_w}{\frac{1}{2}\rho U_\infty^2} = 2.5410e-04 \tag{5.45}$$

The exact solution has a thickness of $\delta_{0.99} = 3.6e-04$ at $x = 1.05$. If we set

$$\frac{\delta_{0.99}}{\Delta y} = 4 \quad \xrightarrow{yields} \quad \Delta y = \frac{\delta_{0.99}}{4} = 9.0e-05 \tag{5.46}$$

then $\Delta y = 9.0e-05$ is set as a grid size to calculate skin frictions for different orders of CPR formulation at $x = 1.05$. In this case, there are 4 cells inside the boundary layer. 5th order CPR formulation's result is very close to the exact result.

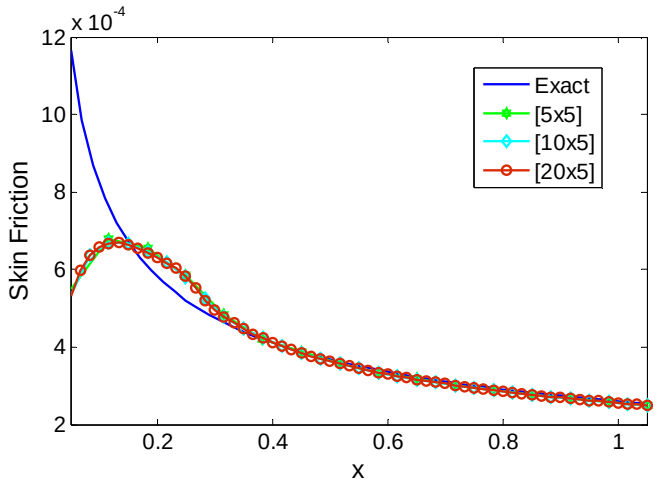

Figure 5.5. Skin frictions comparison with different grids in x-direction for 4th order CPR

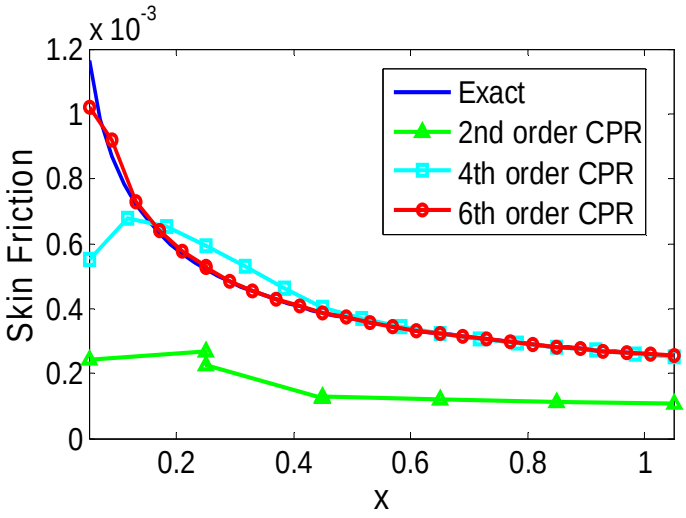

Fig 5.6. Skin friction comparison with different order CPR formulation for grid [5 × 5]

If we set 2 cells inside the boundary layer

$$\frac{\delta_{0.99}}{\Delta y} = 2 \quad \xrightarrow{yields} \quad \Delta y = \frac{\delta_{0.99}}{2} = 1.8e-04 \tag{5.47}$$

$\Delta y = 1.8e-04$ is set as a grid size to calculate the Skin frictions for different orders of CPR formulation at $x = 1.05$ in table 5.14. 5th order CPR formulation provides a result close to the exact solution.

Table 5.13 Skin frictions comparison

with $\Delta y = 9.0e-05$

	2nd order CPR	3rd order CPR	4th order CPR	5th order CPR	6th order CPR
Δy	9.0e-05	9.0e-05	9.0e-05	9.0e-05	9.0e-05
SF	1.7962e-04	2.4734e-04	2.5371e-04	2.5410e-04	2.5411e-04
Error(%)	29.31%	2.66%	0.15%	0%	0%

Table 5.14 Skin frictions comparison

with $\Delta y = 1.8e-04$

	2nd order CPR	3rd order CPR	4th order CPR	5th order CPR	6th order CPR
Δy	1.8e-04	1.8e-04	1.8e-04	1.8e-04	1.8e-04
SF	1.1534e-04	2.1569e-04	2.4792e-04	2.5418e-04	2.5411e-04
Error(%)	54.60%	15.12%	2.43%	0.03%	0.0004%

CHAPTER 6. CONCLUSION AND FUTURE WORK

The CPR (Correction Procedure via Reconstruction) method with a hybrid discontinuous space is studied. The hybrid space includes polynomial and Fourier bases. Although the piecewise polynomial bases are general used as local spaces in most discontinuous methods, they may not always provide the best approximation to the solutions for some specific problems. For the boundary layer problems, exponential functions achieved better results than the classic polynomial functions due to the large slope of the solution near the boundary. For the highly oscillatory problems, the trigonometric functions provide better approximation because of high wave numbers. In our proposed method, hybrid bases are applied. The polynomial bases are used in order to keep a certain order of accuracy, on the other hand the Fourier bases are applied with the objective of resolving broad-band wave propagation. Due to Fourier spaces, the exact dispersion relation $\Omega = K$ is exactly satisfied at a certain K. Free-parameters are optimized to minimize both dispersion and dissipation errors. This method is named as frequency optimized CPR formulation (FOCPR).

In the one-dimensional analysis, free-parameters in the Fourier bases are optimized to minimize both dispersion and dissipation errors by mimicking the similar idea of dispersion-relation-preservation (DRP) to maximize the resolvable wave number given a certain error threshold. The hybrid bases with optimized free-parameters show good wave propagation properties. A comparison was made with the dispersion and dissipation properties of the central and upwind DRP schemes in 1D. The four-point stencil optimized hybrid bases of CPR formulation is able to resolve waves with non-dimensional wave numbers as high as the

seven-point stencil central and upwind schemes. The more Fourier bases components are used, the less dispersion and dissipation errors the schemes show.

Mesh resolution analysis is applied to verify the optimization of the hybrid bases. The number of grid points per wavelength (PPW) is presented with the objective of accurately simulating wave propagation over larger distance. The PPW analysis matches the optimization perfectly, and both methods can be used to verify each other. More Fourier terms are there, the fewer PPW are required. Because the optimized schemes are optimized for a given range of wave number, they required fewer PPW if the propagation distance is relative short. As the number of wavelength traveled increase, the advantage of the optimized schemes diminished as the required PPW increase. However if fewer PPW is required, the use of optimized scheme not only gives most accurate results but also results in significant saving of CPU time.

In the two-dimensional analysis, the tensor product bases are applied for the quadrilateral grids. The accuracy of the hybrid bases depends on different non-dimensional wave numbers. Both the dispersion and dissipation errors are largest in the direction of $\theta = 0$ or $\theta = \pi/2$. The dispersion relation in the direction $\theta = 0$ or $\theta = \pi/2$ is the same as the corresponding one-dimensional analysis.

Several numerical tests are given to verify the wave propagation analysis. The designed spaces for CPR formulation exactly simulate the one-dimensional wave equation with a sine wave as the initial condition at some specific non-dimensional wave number. The method has been tested for Problem 1 in Category 1 (C1P1) on benchmark problem in the Fourth Computational Aeroacoustics (CAA) Workshop. It is shown that the scheme with optimized Fourier bases can resolve waves more accurately than the polynomial bases at 3.7 PPW. An

artificial “broadband” wave composes short, medium and long waves is used as an initial condition for the wave equation. The numerical results agree with the PPW analysis. The hybrid base performs better than the corresponding polynomial bases in some conditions. 2D acoustic wave problem is tested. It is verified again that the advantage of the optimized hybrid bases depend on the non-dimensional wave numbers.

Extensive resolution studies were carried out for both 1D and 2D viscous burgers equations with the designed exact solutions to investigate the skin frictions for various order CPR formulation. For CPR method, two different formulations for the diffusion equations are studied. The first formulation is BR1 [9] formulation, the other formulation is the local Galerkin method (LDG) [21]. BR1 formulation did not match the expected the order of accuracy, while the LDG achieves $(k+1)th$ order of accuracy with a degree p polynomial reconstruction.

For 1D viscous burger equation, the skin frictions are studied as the resolution study criteria. For node center 2nd order finite volume method, the skin friction is equal to 0.9034 when $y^+ = 1$. For the 6th order CPR formulation y^+ is equal to 39.6322, if the same skin friction is required. For cell center 2nd order finite volume method when skin friction is equal to 0.9784, $y^+ = 1$. For the 6th order CPR formulation when skin friction is equal to 0.9784, y^+ can reach 23.6351. All of calculation is based on polynomial reconstruction and uniform point distribution within each element of CPR formulation. Different point distribution for CPR formulation is studied. When the points approach to the interface of each element, the better resolution results are obtained. Convergence histories show that the convergence is becoming slow when the points are close to the element interface as a compromise for the more accurate numerical results.

2D viscous burgers equation with an exact solution is designed to test the resolution for various order of CPR formulation. Method of manufactured solutions (MMS) provides a general exact solution for accuracy verification. In MMS, instead of solving original equation directly, the equation with an analytical source term is solved. For this 2D equation, tensor products of one-dimensional polynomial and rectangular meshes are applied. The errors study shows that the approach is capable of achieving the $(k+1)th$ order of accuracy with a degree k polynomial reconstruction.

Numerical skin frictions are presented with various grids compared with the skin frictions from the exact solution. The finer grids gave better numerical results. And numerical skin frictions are presented for various order CPR formulation compared with the exact skin frictions. For our 2D benchmark problem, the error friction can achieve about 0.15% for 4^{th} order CPR, when cells put inside the boundary layer at $x = 1.05$ and the skin friction is equal to the exact solution when 5^{th} order of CPR formulation is applied, if there are 4 cells inside the boundary layer. If 2 cells inside the boundary layer at $x = 1.05$, the error of skin friction for 5^{th} order of CPR formulation is 0.03%.

APPENDIX A. DISCONTINUOUS GALERKIN METHOD

The discontinuous Galerkin (DG) method is briefly reviewed in the present appendix. Hartmann [39] gave a nice overview of DG method, with studies of its stability for different governing convection-diffusion equations and superconvergence properties for certain functional of the DG solution.

A.1 Framework of DG Method

A short summary of the DG methodology is given as follows. The hyperbolic conservation law is considered.

$$\frac{\partial Q}{\partial t} + \nabla \cdot \vec{F}(Q, \nabla Q) = 0 \tag{A.1}$$

where $\vec{F}(Q, \nabla Q)$ is a flux vector. The domain is partitioned into non-overlapping sub-domains $V_i, i = 1, \dots, N$. On each of these cells, a set of basis function $W_{i,j}, j = 1, \cdots, N$, is introduced. Mostly these function are polynomials with a certain maximum degree k, which results in a scheme with order of accuracy $k + 1$. Other functions like e.g., trigonometric and exponential functions can be used as a set of basis functions too. A solution of the form is given as

$$Q_i = \sum_{j=1}^{N} Q_{i,j} W_{i,j} \tag{A.2}$$

$Q_{i,j}$ are the DG solution variables. Applying the weighted residual form to element V_i, we obtain

$$\int_{V_i} W \left(\frac{\partial Q}{\partial t} + \nabla \cdot \vec{F}(Q, \nabla Q) \right) dV = 0 \tag{A.3}$$

Using divergence theorem, (A.3) is

$$\frac{d}{dt}\int_{V_i} WQ\, dV + \int_{\partial V_i} W\vec{F}(Q,\nabla Q)\cdot\vec{n}dS - \int_{V_i} \nabla W\cdot\vec{F}(Q,\nabla Q)\, dV = 0 \qquad (A.4)$$

where ∂V_i is the cell boundary interface and $\vec{n}$ denotes the unit outward normal vector. Since the normal flux is discontinuous across the interface of contiguous domains, a common numerical flux (the Riemann flux in the case of inviscid flow) is used to replace the normal flux based on the solutions and gradients on both element V_i and its neighbor.

$$\vec{F}(Q,\nabla Q)\cdot\vec{n} = \hat{F}(Q_i,\nabla Q_i, Q_{i+},\nabla Q_{i+},\vec{n}) \qquad (A.5)$$

where Q_i and ∇Q_i are the solutions and gradients on V_i, Q_{i+} and ∇Q_{i+} are from the neighboring element. The inviscid flux is the Riemann flux depending on Q_i, Q_{i+} and the unit normal to ensure a coupling between neighboring cells.

A.2 DG Basis Functions

The basis functions $W_{i,j}$ should be specified to fully define a DG scheme. The stability and accuracy properties of the DG method only depend on the choice of the solution approximation space. Mostly, the space of polynomial with degree k or less is chosen, which leads to a $(k+1)th$ order accuracy scheme for convection equations. Any set of complete basis polynomials can be used as basis functions, without changing the stability and accuracy properties of the DG schemes.

Non-polynomial functions can be introduced as basis functions in order to better represent certain physical solutions. Yuan and Shu [109] used trigonometric and exponential functions in order to obtain better numerical results for specific types of PDEs and initial and boundary conditions.

A.3 Viscous Treatment for DG Method

The discretization of diffusive terms with the DG method has been discussed by many researches over the past decade. Different approaches were developed, which include the local DG approach by Cockburn and Shu [28], different approaches by Bassi and Rebay [8-10], interior penalty approaches proposed by Douglas and Dupont [33], the approach of Baumann and Oden [71] and the recovery methods by Van Leer et al. [96]. The interested reader is referred to relative works for detailed description of all these discretization techniques for diffusive terms with the DG method.

APPENDIX B. SPECTRAL VOLUME METHOD

The spectral volume (SV) method is briefly reviewed in this appendix. Readers can refer to [100] to get more details of SV method.

B.1 Framework of SV Method

The SV method uses averages over control volumes (CVs) as solution variables like the FV method. In the SV method, each simplex element V_i called a spectral volume, is partitioned into sub-cells $V_{i,j}$ called control volumes (CVs), as shown in Fig. A.1. We consider the following conservation laws

$$\frac{\partial Q}{\partial t} + \nabla \cdot \vec{F}(Q) = 0 \tag{B.1}$$

Integrating (B.1) on a spectral volume (SV) V_i, we obtain

$$\int_{V_i} \frac{\partial Q}{\partial t} dV + \oint_{\partial V_{i,j}} \vec{F}(Q) \cdot \vec{n} dS = 0 \tag{B.2}$$

$\vec{n}$ is the unit outward normal of $\partial V_{i,j}$. Define the CV averaged conservative variables for V_i as

$$\bar{Q}_{i,j} = \frac{\int_{V_{i,j}} Q dV}{|V_{i,j}|} \tag{B.3}$$

where $|V_{i,j}|$ is the volume of $V_{i,j}$. The (1.20) becomes

$$\frac{d\bar{Q}_{i,j}}{dt} |V_{i,j}| + \sum_{f \in \partial V_{i,j}} \vec{F}(u) \cdot \vec{n} dS = 0 \tag{B.4}$$

f represents the face. $\bar{Q}_{i,j}$ are the DOFs, which are used to construct a degree k polynomial using the following equation

$$Q_i(\vec{r}) = \sum_{j=1}^{m} W_{i,j}(\vec{r})\bar{Q}_{i,j} \tag{B.5}$$

m is the sub-cells number. The "shape function" like polynomials $W_{i,j}(\vec{r})$ associated with $V_{i,j}$ should satisfy

$$\frac{1}{|V_{i,j}|}\int_{V_{i,j}} W_{i,l}dV = \delta_{j,l} \tag{B.6}$$

where $\delta_{j,l}$ is the Kronecker delta. If the solution is sufficiently smooth, the polynomial is an $(k+1)th$ order approximation of the solution. The reconstruction solutions are generally not continuous on the interface between two SVs, so a Riemann flux is used to take place the normal flux in this inviscid case.

$$\frac{d\bar{Q}_{i,j}}{dt}|V_{i,j}| + \sum_{f\in\partial V_{i,j}}\int_f \hat{F}(Q, Q_+, \vec{n})dS = 0 \tag{B.7}$$

Since the solution is continuous inside the SV, the analytical fluxes are used for interior faces. The surface integral is computed using $(k+1)th$ order Gauss quadrature formula, which is exact for degree k or less polynomials. If the governing equations are linear, the surface integral can be computed exactly because the flux vector is also a degree k polynomial.

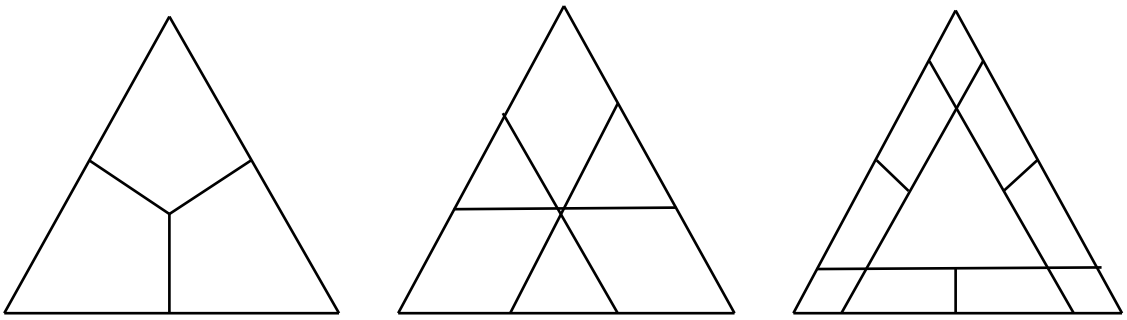

(a) (b) (c)

Figure B.1 Control volumes for (a) linear; (b) quadrature; (c) cubic SV in a triangle

B.2 SV Basis Functions

Mostly, the space of polynomial with degree k or less is chosen like Lagrangian polynomials, with respect to CV-averaged values instead of pointwise values. This means that in general, the SV basis polynomials depend on the local geometry of the corresponding cell. Non-polynomial functions can also be introduced as basis functions like DG method.

B.3 Viscous Treatment for SV Method

Different treatments for the diffusive terms with the SV method are known in literature [79]. Most of them are derived from similar approaches that were developed for the DG method can be found in Arnold et al. [3]. The most popular three approaches are the local SV (LSV) approach based on the local DG (LDG) approach proposed by Cockburn and Shu [28], the second approach of Bassi and Rebay (BR2) proposed by Bassi and Rebay et al. [8] for DG, and the interior penalty (IP) method, see Douglas and Dupont [33].

APPENDIX C. SPECTRAL DIFFERENCE METHOD

An alternative to the SV method, which was discussed in the previous appendix, the spectral difference (SD) method is briefly reviewed in this appendix. Readers can refer to [63] to get more details of the SD method.

C.1 Framework of SD Method

In a SD method, two sets of grid points, i.e., the solution points and flux points are defined in each element. The solution points are the locations where the nodal values of the conservative variables Q are specified (usually Gauss quadrature points). Flux points are the locations where the nodal values of the fluxes are computed. The DOFs in the SD method are conservative variables at the solutions points. Fig C.1 displays the placements of the solution and flux points for the first to third order SD schemes.

Let the position vector of the jth solution point at cell i be denoted by $\vec{r}_{i,j}$, and the kth flux point at cell i be denote by $\vec{r}_{i,k}$. Denote $Q_{i,j}$ the solution at $\vec{r}_{i,j}$. Given the soltuions at $\vec{r}_{i,j}$, an piecewise degree k polynomial can be constructed using Lagrange-type polynomial basis, i.e.,

$$p_i(\vec{r}) = \sum_{j=1}^{m} L_{i,j}(\vec{r})\, Q_{i,j} \qquad \text{(C. 1)}$$

where $L_{i,j}(\vec{r})$ are the cardinal basis functions. With (C.1), the solutions of Q at the flux points $\vec{r}_{i,j}$ can be computed easily. Since the solutions are discontinuous across element boundaries, the fluxes at the element interface are not uniquely defined. The normal flux can be computed with approximate Riemann solver $\hat{F}(Q_i, Q_{i+}, \vec{n})$. Consider the face flux point

shown in Fig C.2, $\vec{n}_1$is denoted the outgoing normal from cell V_i to cell 1. For this interface point, Q_i is computed from V_i and Q_{i+} is computed from cell 1.

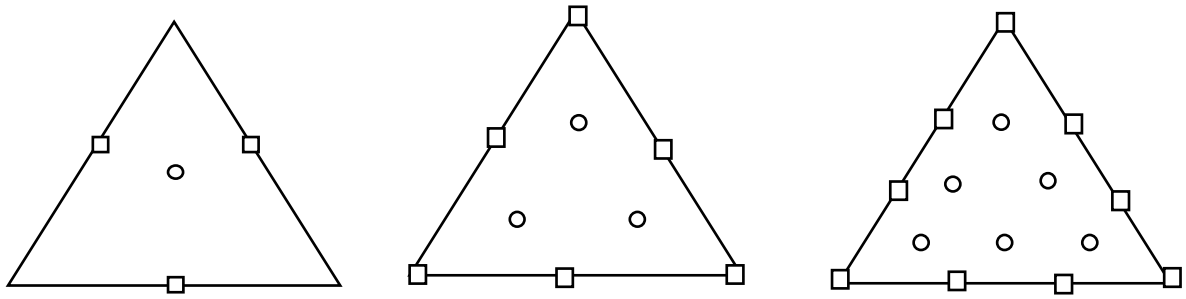

(a) (b) (c)

Figure C.1. Solution (solid circles) and flux points (solid squares) for (a) 1st order (b) 2nd order (c) 3rd order SD in a triangle

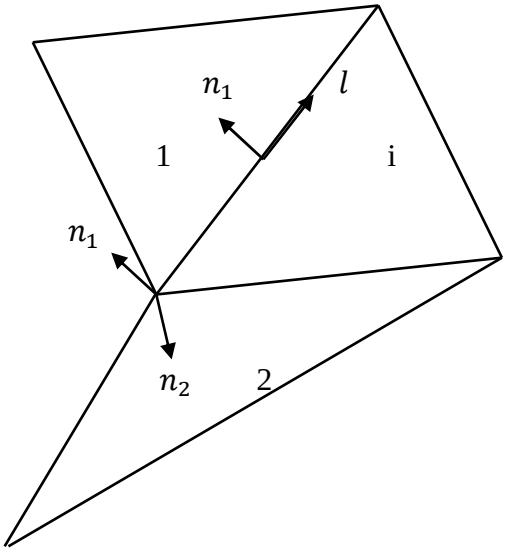

Figure C.2. Illustration of flux computation for face and corner points

Since the tangential component of the flux does not affect the conservation property, we have the complete freedom in determining it at the face point. There are two options to define on the interface. One is to use the average two tangential components from both sides of the

interface, the other is to use its own tangential component. l is the unit vector in the tangential direction.

For a corner flux point in cell V_i, two faces (from cell V_i) share the corner point, as shown in Fig 1.4. Let the unit normal of the two faces be $\vec{n}_1$ and $\vec{n}_2$. The normal components of flux $\hat{F}_1$ and $\hat{F}_2$ in $\vec{n}_1$ and $\vec{n}_2$ directions and computed with a 1D Riemann solver in the normal directions. It is important to emphasize here that fluxes at cell corner points do not have unique values for all the cells sharing the corner. In spite of that, local conservation is guaranteed because neighboring cells do share a common normal flux at all the flux points. Once the fluxes at all the flux points are recomputed, they are used to form a degree $(k+1)$ polynomial, i.e.,

$$\vec{F}_i(\vec{r}) = \sum_{l=1}^{m_{k+1}} Z_{i,l}(\vec{r})\vec{F}_{i,l} \tag{C.2}$$

where $Z_{i,l}(\vec{r})$ are the set of cardinal basis functions defined by $\vec{r}_{i,l}$ and $\vec{F}_{i,l} = \vec{F}(\vec{r}_{i.l})$. Obviously, the divergence of the flux at any point within the cell can be computed using

$$\nabla \cdot \vec{F}_i(\vec{r}) = \sum_{l=1}^{m_{k+1}} \nabla Z_{i,l}(\vec{r}) \cdot \vec{F}_{i,l} \tag{C.3}$$

To update the solutions at the solution points $\vec{r}_{i,j}$, we need to evaluate the divergence of these points, which can be easily computed according to

$$\nabla \cdot \vec{F}_i(\vec{r}_{i,j}) = \sum_{l=1}^{m_{k+1}} \nabla Z_{i,l}(\vec{r}_{i,j}) \cdot \vec{F}_{i,l} \tag{C.4}$$

Finally the semi-discrete scheme to update the solution unknowns can be written as

$$\frac{dQ_{i,j}}{dt} + \sum_{l=1}^{m_{k+1}} \nabla Z_{i,l}(\vec{r}_{i,j}) \cdot \vec{F}_{i,l} = 0 \tag{C.5}$$

The SD method for quadrilateral or hexahedral grid is similar to the staggered grid multi-domain spectral method [58]. It is particularly attractive because all the spatial operators are 1D in nature. In 2D, the solution and flux points are usually the Gauss and Gauss-Lobatto points. An obvious advantage of the SD method is that the formulation (C.5) does not involve any integrals. As a consequence, costly Gauss quadrature rules are avoided.

C.2 SD Basis Functions

In general, the space of polynomial is chosen like Lagrangian polynomials similar to DG and SV method. At the solution and flux points, the polynomial value should be equal to the solution and flux variables, respectively. The SD basis polynomials are thus Lagrangian k order polynomials with respect to the solution points. The flux basis polynomials are also Lagrangian polynomial with $k + 1$ degree. Notice that, unlike the SV basis polynomials, the SD solution and flux basis polynomials are always independent of the coordinate system.

C.3 Viscous Treatment for SD Method

Like with the SV method, the treatment of the diffusive terms with the SD method is derived from approaches that were developed for the DG method. Similar approaches for SV method are applied in SD method, which include the local SD (LSD) approach, corresponding to the LDG scheme for DG [28], the approach of Bassi and Rebay (BR2) [8], and the interior penalty (IP) approach [33].

APPENDIX D. MATRIX DEFINITIONS

In this appendix, we give the matrix that appear in Eqs (3.9) and (4.4) of section 3 and 4.

For the one-dimensional equation (3.1), the upwind Riemann flux formulation ($\alpha = 1$) is used. Let the weight function be $\{W_l(\xi)|l = 1,2,\cdots,p+1\}$, where p+1 is the DOFs in each element, and ξ is the local coordinate $\xi \in [-1,1]$. The matrices in Eq. (3.9) are formed as

$$N_{mj}^{-1} = -2 * G^{-1} * W_m(-1)W_j(1), \qquad (m,j = 1,\dots,p+1) \tag{D.1}$$

$$N_{mj}^{0} = 2 * \frac{\partial W_j(\xi_m)}{\partial \xi} + 2 * G^{-1} * W_m(-1)W_j(-1), \qquad (m,j = 1,\dots,p+1) \tag{D.2}$$

G^{-1} is the inversion matrix of G, and $G_{m,j} = \int_{-1}^{1} W_m(\xi)\, W_j(\xi) d\xi \;\; (m,j = 1,\cdots,p+1)$.

For the two-dimensional equation (4.1), the upwind Riemann flux formulation is also used. The matrices in Eq. (4.4) are given as follows

$$N_{ij}^{-1} = a_x \begin{cases} 0 & if\ f1\left(\frac{i-1}{p+1}\right) \neq f1\left(\frac{i-1}{p+1}\right) \\ -2 * G^{-1} * W_{f2(i,p+1)}(-1)W_{f2(j,p+1)}(1), & if\ f1\left(\frac{i-1}{p+1}\right) = f1\left(\frac{i-1}{p+1}\right) \end{cases} \tag{D.3}$$

$N_{ij}^{0} =$

$$a_x \begin{cases} 0 & if\ f1\left(\frac{i-1}{p+1}\right) \neq f1\left(\frac{i-1}{p+1}\right) \\ 2 * \frac{\partial W_j(\xi_{f2(i,p+1)})}{\partial \xi} - 2 * G^{-1} * W_{f2(i,p+1)}(-1)W_{f2(j,p+1)}(-1), & if\ f1\left(\frac{i-1}{p+1}\right) = f1\left(\frac{i-1}{p+1}\right) \end{cases} \tag{D.4}$$

$$M_{ij}^{-1} = a_y \begin{cases} 0 & if\ f2\left(\frac{i-1}{p+1}\right) \neq f2\left(\frac{i-1}{p+1}\right) \\ -2 * G^{-1} * W_{f1(i,p+1)}(-1)W_{f1(j,p+1)}(1), & if\ f2\left(\frac{i-1}{p+1}\right) = f2\left(\frac{i-1}{p+1}\right) \end{cases} \tag{D.5}$$

$$M_{ij}^{0} =$$

$$a_y \begin{cases} 0 & if\ f2\left(\frac{i-1}{p+1}\right) \neq f2\left(\frac{i-1}{p+1}\right) \\ 2 * \frac{\partial W_j(\xi_{f1(i,p+1)})}{\partial \xi} - 2 * G^{-1} * W_{f1(i,p+1)}(-1) W_{f1(j,p+1)}(-1), & if\ f2\left(\frac{i-1}{p+1}\right) = f2\left(\frac{i-1}{p+1}\right) \end{cases} \quad (D.6)$$

where $f1$ denotes the rounded function, such as $floor(i-1, p+1)$ in Matlab. $f2$ is given as

$$f2(i, p+1) = \begin{cases} mod(i, p+1), & if\ mod(i, p+1) \neq 0 \\ p+1, & if\ mod(i, p+1) = 0 \end{cases} \quad (A.7)$$

Where mod is defined as complementation function, such as *mod* in Matlab.

BIBLIOGRAPHY

1. M. Aftosmis, D. Gaitonde, T.S. Tavares, Behavior of linear reconstruction techniques on unstructured meshes, AIAA Journal 1995; 33(11): 2038-2049.
2. W. Kyle Anderson, A grid generation and flow solution method for the Euler equations on unstructured grids, J. Comput. Phys 1994; 110: 23-38.
3. D.N. Arnold, F. Brezzi, B. Cockburn, Marin LD. Unified analysis of discontinuous Galerkin methods for elliptic problems. SIAM. J. Numer. Anal 2001; 39:1749–79.
4. Graham Ashcroft, Xin Zhang, Optimized prefactored compacted schemes, J. Comput. Phys. 190, pp. 459-477 (2003)
5. H.L. Atkin, C.-W. Shu, Qudrature-free implementation of discontinuous Galerkin method for hyperbolic equations. AIAA Journal 1998; 36:775-82.
6. D. Balsara, C.-W. Shu, Monotonicity preserving weighted essentially non-oscillatory schemes with increasing high order of accuracy, J. Comput. Phys. 160, pp. 405-452 (2000).
7. T.J. Barth, D.C. Jespersen, The design and application of upwind schemes on unstructured meshes, AIAA Paper No. 89-0366, 1989
8. F. Bassi, A. Crivellini, D.A. Di Pietro, S. Rebay, An artificial compressibility flux for the discontinuous Galerkin solution of the incompressible Navier-Stokes equations, J. Comput. Phys. 218 (2006) 794-815
9. F. Bassi and S. Rebay, A high-order accurate discontinuous finite element method for the numerical solution of the compressible Navier-Stokes equations, J. Comput. Phys. 131 (1997) 267-279.

10. F. Bassi and S. Rebay, High-order accurate discontinuous finite element solution of the 2D Euler equations. J. Comput Phys 1997; 138:251-285.
11. F. Bassi and S. Rebay, Numerical evaluation of two discontinuous Galerkin methods for the compressible Navier-Stokes equations. Int J Numer Methods Fluids 2002; 40(1):197-207.
12. F. Bassi and S. Rebay, Numerical solution of the Euler equations with a multiorder discontinuous
13. F. Bassi, S. Rebay, G. Mariotti, S. Pedinotti, and M. Savini. A high-order accurate discontinuous finite element method for inviscid and viscous turbomachinery flows. In R. Decuypere and G. Dibelius, editor, *Proceedings of 2nd European Conference on Turbomachinery*, pages 99–108, Antwerpen, Belgium, 1997.
14. C.E. Baumann, T.J. Oden, A discontinuous hp finite element method for convection-diffusion problems. Comput. Methods Appl. Mech. Engrg., 175:311–341, 1999.
15. C.E. Baumann, T.J. Oden, A discontinuous hp finite element method for the Euler and Navier–Stokes equations. Int J Numer Methods Fluids 1999; 31(1):79–95.
16. R. Biswas, K.D. Devine, J.E. Flaherty, Parallel adaptive finite element methods for conservation laws, Appl Numer Math, 1994; 14: 255-283.
17. J.P. Boris, D.L. Book, Flux corrected transport, 1 SHASTA, A fluid transport algorithm that works, J Comput Phys A 1973; 11: 38-69.
18. Q.-Y. Chen. Partitions for Spectral (Finite) Volume Reconstruction in the Tetrahedron. J. Sci. Comput., 29(3):299–319, 2006.
19. Q.-Y. Chen. Partitions of a simplex leading to accurate spectral (finite) volume reconstruction. SIAM J. Sci. Comput., 27(4):1458– 1470, 2006.

20. S. Christofi, The study of building blocks for essentially non-oscillatory (ENO) schemes, Ph.D thesis, Division of Applied Mathematics, Brown University, 1996.
21. B. Cockburn, G.E. Karniadakis, C.-W. Shu, The development of discontinuous Galerkin methods. In : Cockburn B, Karniadakis GE, Shu CW, editor. Berlin: Springer; 2000.
22. B. Cockburn, Shu C-W. TVB Runge-Kutta local projection discontinuous Galerkin finite element method for conservation laws II: general framework. Math Comput 1989; 52:411-35.
23. B. Cockburn, S Hou, C.-W. Shu. TVB Runge-Kutta local projection discontinuous Galerkin finite element method for conservation laws IV: the multidimensional case. Math Comput 1990; 54:545-81.
24. B. Cockburn, S-Y Lin, C.-W. Shu, TVB Runge-Kutta local projection discontinuous Galerkin finite element method for conservation laws III: One-dimensional systems. J Comput Phys 1989; 84:90-113.
25. B. Cockburn and C.-W. Shu, The Runge-Kutta local projection P^1 Discontinuous Galerkin finite element method for scalar conservation laws, In proceedings of First Fluid Dynamics Congress, University of Minnesota, Institute for Mathematics and its Applications Preprint Series # 388, July 1988.
26. B. Cockburn and C.-W. Shu, TVB Runge-Kutta local projection discontinuous Galerkin finite element method for conservation laws II: general framework, Math. Comput., 52:411-435, 1989, 7, 221
27. B. Cockburn, C.-W. Shu. The Runge-Kutta discontinuous Galerkin finite element method for conservation laws V: multidimentional systems. J Comput Phys 1998; 141:199-224.

28. B. Cockburn and C.-W. Shu, the local discontinuous Galerkin method for time-dependent convection diffusion systems, SIAM J. Numer. Anal., 35 (1998), pp. 2440-2463.

29. B. Cockburn and C.-W. Shu, Runge-Kutta discontinuous Galerkin methods for convectin-dominated problems,J. Sci. Comput., 16(3):173-261, 2001. 8

30. B. Cockburn, F. Li, C.-W. Shu, Locally divergence-free discontinuous Galerkin methods for the Maxwell equations, J. Comput. Phys 194 (2004) 588-610

31. Bruno Costa[a,] and Wai Sun Don[b], Multi-domain hybrid spectral-WENO methods for hyperbolic conservation laws , J. compu phys. 224, pp. 970 – 991 (2007).

32. V. Dolejsi, on the discontinuous Galerkin method for numerical solution of the Navier-Stokes equations, Int. J. Numer. Meth. Fluids. 45, pp 1083-1106 (2004)

33. J. J. Douglas and T. Dupont. Interior Penalty Procedures for Elliptic and Parabolic Galerkin Methods, In lecture Notes in Phys. 58, Berlin, 1976

34. John A. Ekaterinaris, High-order accurate, low numerical diffusion methods for aerodynamics, progress in Aerospace Sciences 41 (2005) 192-300

35. T. Haga, N. Ohnishi, K. Sawada, A. Masunaga, Spectral volume computation of flowfield in aerospace application using earth simulator. AIAA Paper No. 2006-2823, 2006

36. R. Harris, Z.J. Wang, Y. Liu, Efficient implementation of high-order spectral volume method for multidimensional conservation laws on unstructured grids, AIAA Paper No. 2007-912, 2007.

37. A. Harten, High-resolution schemes for hyperbolic conservation laws, J Comput Phys 1983; 49: 357-393.

38. R. Hartmann and P. Houston, Symmetric interior penalty DG methods for the compressible Navier-Stokes Equations I: Method formulation, Int. J. Numer. Anal. Model. 3(1), pp. 1-20, (2006)

39. R. Hartmann, 35th CFD/ADIGMA Course on Very High Order Discretization Methods, Chapter numerical analysis of higher order discontinuous Galerkin finite element methods, Von Karmann Institute for Fluid Dynamics, October 2008.

40. O. Hassan, K. Morgan, J. Peraire, An implicit finite element method for high speed flows, AIAA Paper No. 90-0402, January 1990.

41. R. Hixon, A new class of compact schemes, AIAA Paper, No. 98-0367, 1998.

42. Changqing Hu, C.-W. Shu, Weighted essentially Non-oscillatory schemes on Triangular mehses, J. Comput. Phys, 150, pp. 97-127 (1999).

43. Fang Q. Hu, M. Y. Hussaini, Patrick Rasetarinera, An analysis of the discontinuous Galerkin method for wave propagation problems, J. Comput. Phys. 151 (1999) 921-946

44. P. G. Huang, Z. J. Wang, and Y. Liu. An implicit space-time spectral difference method for discontinuity capturing using adaptive polynomials, AIAA paper, 2005-5255, 2005

45. TJR. Hughes, Recent progress in the development and understanding of SUPG methods with special reference to the compressible Euler and Navier-Stokes equations, Int J Numer Methods Fluids, 1987; 7: 1261-1275

46. TJR. Hughes, LP. Franca, GM. Hulbert, A new finite element formulation for computational fluid dynamics: VIII. The Galerkin least squares method for advective-diffusive equations, Comput Methods Appl Mech Eng 1989; 73: 173-189

47. TJR. Hughes, M. Mallet, A new finite element formulation for CFD: IV. A discontinuity-capturing operator for multidimensional advective-diffusive systems, Comput methods Appl Mech Eng 1986; 58(3): 329-356

48. H.T. Huynh. An upwind moment scheme for conservation laws. in: Groth, Zingg, editors. Proceedings of the third international conference of CFD, Toronto, Canada, 2004.

49. H.T. Huynh, A flux reconstruction approach to high-order schemes including discontinuous Galerkin methods, AIAA paper 2007-4079.

50. H.T. Huynh, A reconstruction approach to high-order schemes including discontinuous Galerkin for diffusion, AIAA-2009-403

51. Henry Martin Jurgens, High-accuracy finite-difference schemes for linear wave propagation, Ph.D thesis, Department of Aerospace Science and Engineering, University of Toronto, 1997.

52. M.K. Kadalbajoo, K.C.Patidar, Exponentially fitted spline in compression for the numerical solution of singular perturbation problems, Computers and mathematics with Applications 46 (2003) 751-767.

53. R. Kannan, Y. Sun, and Z. J. Wang. A Study of Viscous Flux Formulations for an Implicit P-Multigrid Spectral Volume Navier-Stokes Solver, AIAA paper, 2008-783, 2008

54. Aaron Katz and Venkateswaran Sankaran, Mesh quality effects on the accuracy of CFD solutions on unstructured meshes, AIAA 2010

55. C. M. Klaij, J. J. W. van der Vegt, and H. van der Ven. Space-time discontinuous Galerkin method for the compressible Navier-Stokes equations. J. Comput. Phys., 217(2):589–611, 2006.

56. D.D. Knight, Elements of numerical methods for compressible flow, Cambridge: Combridge University Press; 2006

57. D. A. Kopriva. A conservative staggered-grid Chebyshev multidomain method for compressible flows, II semi-structured method. J. Comput. Phys., 128(2):475–488, 1996.

58. D. A. Kopriva and J. H. Kolias. A conservative staggered-grid Chebyshev multidomain method for compressible flows, J. Comput. Phys., 125(1):244–261, 1996.

59. Lilia Krivodonova, Marsha Berger, High-order accurate implementation of solid wall boundary conditions in curved geometries. J Comput Phys 2006; 211(2):492–512.

60. R.J. Leveque, Finite volume methods for hyperbolic problems, Cambridge: Cambridge University Press; 2002

61. Yuguo Li, Wavenumber-Extended High-Order Upwind-Biased Finite-Difference Schemes for Convective Scalar Transport, J. Comput. Phys. 133, 235-255 (1997)

62. S.Y. Lin and Y.S. Chin, Discontinuous Galerkin finite element method for Euler and Navier–Stokes equations. AIAA J 1993; 31(11):2016–26.

63. Yen Liu, Marcel Vinokur, and Z.J. Wang, Discontinuous spectral difference methods for conservation laws on unstructured grids, in C. Groth and D.W. Zingg (Eds.), Proceeding of the 3rd international conference in CFD, Toronto, Springer, 2004, pp. 449-454

64. Yen Liu, Marcel Vinokur, and Z.J.Wang, Spectral (finite) volume method for conservation laws on unstructured grids V: extension to three-dimensional system, J. Comput. Phys, 2006; 212: 454-472

65. Yen Liu, Marcel Vinokur, and Z.J.Wang, Spectral difference methods for unstructured grids I. Basic formulation, J. comput phys. 216, pp. 780-801 (2006)

66. R. Lohner, K Morgan, OC. Zienkiewicz, An adaptive finite element procedure for compressible high speed flows, Comput Methods Appl Mech Eng 1985; 51: 441-465

67. Igor Lomtev and G.E. Karniadakis. A discontinuous Galerkin method for the Navier–Stokes equations. Int J Numer Methods Fluids 1999; 29(5):587–603.

68. R.B. Lowrie, P.L. Roe and B. Van Leer, A space-time discontinuous Galerkin method for the time accurate numerical solution of hyperbolic conservation laws. AIAA Paper No. 95–1658, 1995.

69. Remaki Malika, Habashi W.G. A discontinuous Galerkin method/HLLC solver for the Euler equations. Int J Numer Methods Fluids 2003;43(12):1391–405.

70. G. May and A. Jameson. A spectral difference method for the Euler and Navier-Stokes equations. AIAA paper, 2006-304, 2006.

71. T.J. Oden, Ivo Babuska, C.E. Baumann, A discontinuous hp finite element method for diffusion problems. J Comput Phys 1998; 146(2):491–519.

72. J. Peraire and P.-O.Persson, The compact discontinuous Galerkin (CDG) method for elliptic problems, SIAM J.Sci. Comput. 30, pp. 1806-1824 (2008)

73. Y.N. Reddy, P.P. Chakravarthy, An exponentially fitted finite difference method for singular perturbation problems, Applied mathematics and Computation, 154 (2004) 83-101.

74. W.H. Reed and T.R. Hill, Triangular mesh methods for the neutron transport equation, Technical Report LA-UR-73-479, Los Alamos Scientific Laboratory; 1973

75. Patrik J. Roache, Code verification by the method of manufactured solutions, Transactions of the ASME, Vol. 124, 2002, pp. 4-10

76. Hai-qing Si[a,*], Tong-guang Wang[b], Grid-optimized upwind dispersion-relation-preserving scheme on non-uniform Cartesian grids for computational aeroacoustics, Aerospace Science and Technology 12 (2008) 608-617.

77. J.L. Steger, R.F. Warming, Flux vector splitting of the inviscid gas dynamics equations with application to finite difference methods; J Comput Phys 1981; 40: 263

78. Huafei Sun, David L.Darmofal, and Robert Haimes, On the impact of triangle shapes for boundary layer problems using high-order finite element discretization, AIAA 2010-542

79. Yuzhi Sun and Z.J. Wang, Formulations and analysis of the spectral volume method for the diffusion equation, Communications in numerical methods in engineering, 20:927-937 (2004)

80. Yuzhi Sun, Z.J.Wang, High-order spectral volume method for the Navier-Stokes equations on unstructured grids, AIAA 2004-2133

81. Yuzhi Sun, Z.J.Wang, Yen Liu, Spectral (finite) volume method for conservation laws on unstructured grids VI: Extension to viscous flow, Journal of Computational Physics 215 (2006) 41-58

82. Yuzhi Sun, Z.J.Wang, Evaluation of discontinuous Galerkin and spectral volume methods for scalar and system conservation laws on unstructured grid, Int J Numer Methods Fluids, 2004; 45(8):819-838

83. Y. Sun, Z. J. Wang, and Y. Liu. High-order Multidomain Spectral DifferenceMethod for the Navier-Stokes Equations on Unstructured Hexahedral Grids. Commun. Comput. Phys., 2(2):310–333, 2007.

84. C. K. W. Tam, Computational Aeroacoustics: Issues and Methods , AIAA Journal, Vol. 33, No. 10, 1995, pp. 1788-1796

85. C. K. W. Tam and J. C. Webb, Dispersion-Relation-Preserving Finite Difference Schemes for Computational Acoustics, J. Comput. Phys. 107 (1993) 262-281.

86. Kris Van Den Abeele, Tim Broeckhoven, Chris Lacor, Dispersion and dissipation properties of the 1D spectral volume method and application to a p-multigrid algorithm, J. Comput. Phys. 224 (2007) 616-636.

87. Kris Van den Abeele [*,1], Chris Lacor, An accuracy and stability study of the 2D spectral volume method, J. Comput. Phys. 226, pp 1007-1026, (2007)

88. K. Van den Abeele, G. Ghorbaniasl, M. Parsani, and C. Lacor. A stability analysis for the spectral volume method on tetrahedral grids, J. Comput. Phys., 228:257–265, 2009.

89. Kris Van den Abeele, Chris Lacor, Z.J. Wang, on the connection between the spectral volume and the spectral difference method, J. Comput. Phys. 227 (2007) 877-885

90. K. Van den Abeele, C. Lacor, and Z. J.Wang. On the stability and accuracy of the spectral difference method. J. Sci. Comput., 37(2):162– 188, 2008.

91. K. Van den Abeele, M. Parsani, and C. Lacor. An Implicit spectral difference Navier-Stokes solver for unstructured hexahedral grids, AIAA paper, 2009-0181:1–18, 2009.

92. Kris Van den Abeele, Development of high-order accurate schemes for unstructured grids, Ph.D thesis, Department of Mechanical Engineering, Vrije Universiteit Brussel, Belgium, (2008)

93. J.J.W. Van der Vegt, H. Van der Ven, Space time discontinuous Galerkin finite element method with dynamic grid motion for inviscid compressible flows: I. General formulation. J Comput Phys 2002; 182(2):546–85.

94. B. Van Leer, Towards the ultimate conservative difference scheme. IV. A new approach to numerical convection. J. Comput. Phys., 23:276-299,1977.

95. B. Van Leer and M. Lo. Unification of Discontinuous Galerkin methods for Advection and Diffusion. AIAA paper, 2009-0400, 2009.

96. B. Van Leer, M. Lo, and M. V. Raalte. A Discontinuous Galerkin Method for Diffusion Based on Recovery. AIAA paper, 2007-4083, 2007.

97. B. Van Leer and S. Nomura. Discontinuous Galerkin for Diffusion. *AIAA paper*, 2007-5108, 2005.

98. Dolejsi Vit. On the discontinuous Galerkin method for the numerical solution of the Navier–Stokes equations. Int J Numer Methods Fluids 2004; 45(10):1083–106.

99. Z. J. Wang* and R. F. Chen, Optimized Weighted Essentially Nonoscillatory Schemes for Linear Waves with Discontinuity, J. Comput. Phys. 174 (2001) 381-404

100. Z.J. Wang, Spectral (finite) volume method for conservation laws on unstructured grids: basic formulation, J. Comput. Phys. 178 (2002) 210–251

101. Z.J. Wang, Yen Liu, Spectral (finite) volume method for conservation laws on unstructured grids II: extension to two-dimensional scalar equation, J. Comput. Phys. 179, pp. 665 – 697 (2002)

102. Z. J. Wang and Y. Liu. Spectral (finite) volume method for conservation laws on unstructured grids III: One dimensional systems and partition optimization. J. Sci. Comput., 20:137–157, 2004.

103. Z. J. Wang, L. Zhang, and Y. Liu. Spectral (finite) volume method for conservation laws on unstructured grids IV: Extension to two-dimensional Euler equations, J. Comput. Phys., 194(2):716–741, 2004.

104. Z.J. Wang, Yen Liu, The spectral difference method for the 2D Euler equation on unstructured grids, AIAA Paper No. 2005-5112 (2005)

105. Z. J. Wang and Y. Liu. Extension of the spectral volume method to high-order boundary representation. *J. Comput. Phys.*, 211:154– 178, 2006.

106. Z.J. Wang, High-order methods for the Euler and Navier-Stokes equations on unstructured grids, Progree in Aerospace Sciences 43 (2007) 1-41

107. Z. J. Wang[1] and Haiyang Gao[2], A Unifying Lifting Collocation Penalty Formulation for the Euler Equations on Mixed Grids, AIAA 2009-401.

108. Z. J.Wang, Y. Sun, C. Liang, and Y. Liu. Extension of the SD method to viscous flow on unstructured grids. In Proceedings of the 4th international conference on computational fluid dynamics, Ghent,Belgium, July 2006

109. Ling Yuan, C-W. Shu*, Discontinuous Galerkin method based on non-polynomial approximation spaces, J. Comput. Phys. 218 (2006) 295-323.

110. D.W. Zingg, A review of high-order and optimized finite difference methods for simulating linear wave phenomena, AIAA Paper 97-2088

111. M. Zhuang* and R. F. Chen, Optimized Upwind Dispersion-Relation-Preserving Finite Difference Scheme for Computational Aeroacoustics, AIAA Journal. Vol. 36, No. 11, November 1998.

112. M. Zhuang and R.F.Chen, Application of high-order optimized upwind schemes for computational aeroacoustics, AIAA Journal, Vol. 40, No.3, March 2002.

113. Mengping Zhang and C.-W. Shu, An analysis of three different formulations of the discontinuous Galerkin method for diffusion equations, dedicated to professor Jim Douglas, Jr. on the occasion of his 75th birthday.

114. M. Zhang and C.-W. Shu, An analysis and a comparison between the discontinuous Galerkin method and the spectral finite volume methods. Comput Fluids 2005; 34(4-5): 581-592.